Nonlinear Optics in III-V Quaternary Semiconductor Waveguides

Shayan Saeidi

Thesis submitted in partial fulfillment of the requirements for the

MASTER OF APPLIED SCIENCE

degrees in Electrical and Computer Engineering

Supervised by
Professor Ksenia Dolgaleva

Ottawa-Carleton Institute for Electrical and Computer Engineering
University of Ottawa
December, 2017

Abstract

The fundamental limits of electronic systems in communication networks motivated scholars to think of an alternative approach to overcome problems such as demand for wider bandwidths and heat dissipation. All-optical signal processing is demonstrated as a potential solution. A major improvement in cost and speed of networking systems is expected through replacing microelectronics by photonic chips. However, the variety of operations essential to perform all-optical signal processing cannot be handled by a single material platform yet. Several III-V semiconductors, such as AlGaAs, have demonstrated potentials for photonic integration; nevertheless, there is still lack of data in literature on nonlinear optical properties of these materials. In this thesis, we extend the quest to evaluate more candidates from this class of semiconductors. Moreover, we are aiming for demonstrating the potentials of various III-V compounds for nonlinear photonics on-a-chip.

In this thesis, we propose several optical waveguide designs based on quaternary III-V semiconductors AlGaAsSb and InGaAsP. We present modal analysis for waveguide designs and show that effective mode area much less than 1 μm^2 can be obtained. We also report specific waveguide designs that display zero-dispersion points at the specific wavelength ranges of interest. The designed waveguides are thus expected to demonstrate efficient nonlinear optical interactions. Next step is the fabrication of these devices with the goal to experimentally assess their nonlinear optical performance. The fabrication process of InGaAsP/InP strip-loaded waveguide is briefly reviewed. Following that, we report on the first, to the best of our knowledge, demonstration of third-order nonlinear optical interactions in InGaAsP/InP strip-loaded

waveguides. We have performed self-phase modulation, nonlinear absorption measurements, and four-wave mixing experiments at the telecom wavelength range. The nonlinear phase shift up to 2.5 π has been observed.

Following that, we use Monte-Carlo method for design optimization and tolerance analysis of a multi-step lateral taper Spot-Size Converter in indium phosphide. An exemplary four-step lateral taper design featuring 0.35 dB coupling loss at optimal alignment of a standard single-mode fiber, >7 μm 1-dB displacement tolerance in any direction of in a facet plane, and a great stability against manufacturing variances demonstrated.

Acknowledgments

First and foremost, I would like to thank my supervisor Dr. Ksenia Dolgaleva for providing me with the opportunity of working on this research, and patiently guiding me through my studies. I have gained invaluable experiences being a member of her research team and always felt supported during my studies.

I would also like to thank my fellow labmates who were involved in the progress of this research. Kashif M. Awan who contributed to this research with fabrication of the devices, as discussed in Chapter 4. Payman Rasekh who helped me with the experimental setup, as discussed in Chapter 5. I could not pursue my work as discussed in Chapter 6, without help and supervision of Dr. Valery Tolstikhin. Thanks to all my friends in Iran and Canada. Their company and amity means a lot to me.

Needless to say, I must express my profound gratitude to my family, my siblings Negar and Salar and my parents Mina and Hamidreza, for their love, support and encouragement. This accomplishment would not have been possible without them.

Table of Contents

List of Figures

List of Tables

Chapter 1

Introduction

1.1 Motivation

The breakthroughs in the field of Information Technology since the inception of the Internet opened up new ways of generation, storage and transmission of massive amount of data. Recent advances in computer networks along with growing demand of bandwidth-hungry applications such as video sharing and data collection systems, has created the demand for higher bandwidth capacities in signal processing. For instance, according to Cisco Forecast, only monthly global mobile data traffic will be 49 exabytes within the next 5 years, and annual traffic will surpass half zettabyte, while mobile will represent only 20 percent of IP traffic by then [1]. Aside from that, the process sizes in electronic systems is hitting their fundamental limits of a few nanometers which aggravates the problem of heat dissipation. Thsnks to its potentials with overcoming the fundamental limits of electronics, all-optical signal processing has been considered as a viable resolution of the problems associated with electronic bandwidth bottleneck of 40 GHz [2, 3].

Currently, in many data networks, different techniques of electronic signal processing are being implemented which requires converting the signal from optical to

electrical, and then back to optical domain, which is expensive and largely unnecessary. All-optical signal processing can potentially liberate us from our dependence on electronics since the optical signals can be processed in the optical domain without the need of converting them to electrical signals. One of the key operations of all-optical signal processing is all-optical wavelength conversion. It is used to transform optical signal from one wavelength to another without converting them to electrical domain and back. An important motivation to use optical wavelength conversion is that unlike electronic transistors, optical methods do not need to switch every bit of data when handling high bit rates. In optical wavelength conversion, data can be transformed from one wavelength to another at a high pace [4]. This can be achieved by using various nonlinear optical effects such as sum-frequency generation followed by a difference-frequency generation (SFG/DFG), cross-phase modulation (XPM), and four wave mixing (FWM) [5, 6].

All-optical signal processing can be readily achieved by relying on nonlinear optical interactions. That's why nonlinear photonics on-a-chip is an important subject of research and development. However, one of the main barriers on this route is that no optimal material is chosen yet to perform all necessary functions in order to achieve all-optical signal processing [7]. Hence, progress and advances in materials with higher nonlinearities and devices with efficient nonlinear interactions are the key to all-optical signal processing [8]. Various material platforms have been studied and used to perform all-optical wavelength conversion. Several studies show the advantages of silicon for all-optical signal processing [9–11], although efficient light sources cannot be realized in silicon-based material platform. In such a way, in order to make use of all-optical signal processing in silicon, a hybrid integration of silicon with III-V semiconductors is required, which makes integrated optical circuits complex and expensive. Also, silicon suffer from strong two-photon absorption which leads to free-carrier absorption. This can limit the efficiency and operation speed of the all-optical

devices in silicon.

On the other hand, lithium niobate ($LiNbO_3$) exhibits strong 2^{nd}-order nonlinearity and is suitable for SFG/DFG. The titanium indiffused lithium niobate channel waveguides are very efficient for coupling into fibers because of their large mode size, thus providing very low fiber-to-waveguide insertion loss [6,12,13]. However, they lack the flexibility of design in terms of range of refractive index or wavelengths they can cover. Besides, lithium niobate is not a suitable material platform for laser sources or detectors, and hybrid integration is unavoidable.

Another promising material suitable for all-optical devices is chalcogenide glasses. The optical and physical properties of this class of materials, such as high refractive index along with low linear and nonlinear loss coefficients, make them suitable candidates for all-optical signal processing [14, 15]. However, they are not suitable platfoms for active decives. In addition, fabrication of chalcogenide glasses is complex and expensive.

Among all the studied platforms, compound III-V semiconductors demonstrate the best potentials for nonlinear photonics devices on-a-chip. This has been readily demonstrated with aluminum gallium arsenide (AlGaAs) which is deemed to have exceptional nonlinear optical performance for the Telecom C-band wavelength range [16–18]. The combination of its high Kerr nonlinearity ($n_2 = 1.43\times10^{-17}$ m^2W^{-1} for TM polarization [19]) together with insignificant nonlinear absorption convince scholars to consider it as a promising material for achieving all-optical signal processing. Nevertheless, AlGaAs is only one of the representatives of the class III-V semiconductor compounds. In this Master's dissertation, we extend this quest for more suitable nonlinear optical materials of the class III-V. The next section provides more detail on the motivation behind studying III-V semiconductors.

1.2 III-V Semiconductors

Because of unique optical properties of III-V semiconductor compounds, they have always been the spotlight of attentions, both for academic-scientific scholars, and for industrial representatives. From scientific point of view, this field has led to several Noble Prizes in physics - *e.g.* the Nobel Prize received by Z. Alferov and H. Kroemer for their pioneering work in developing semiconductor heterostructures in optoelectronics (2000) [20], and the Nobel Prize awarded to I. Akasaki, H. Amano, and S. Nakamura for the invention of efficient blue light-emitting diodes, enabling bright and energy-saving white light sources (2014) [21]. On the application side, the industrial semiconductor market was worth 43 billion USD in 2016 [22], projected to become more than 50 billion USD in 2018 [23]. In this section, we intend to explain why III-V semiconductor compounds deserve this amount of attention and investment in both science and technology.

This class of semiconductor compounds can be obtained by combining elements from the columns III and V of the pediodic table of chemical elements. Various combinations of these elements result in semiconductor compounds with a wide range of valuable optical properties. Most of these semiconductors are capable of emitting light, *i.e.* they are direct-bandgap semiconductors. Moreover, there are different III-V materials with wide range of bandgap wavelengths, from near-UV to near-IR, enabling light sources emitting different wavelengths. Ternary and quaternary compounds, achievable by intermixing binary semiconductors, yield an additional benefit of adjusting the bandgap wavelength, as well as other optical properties, such as refractive index and susceptibilities, over a wide range of values.

Different studies suggest that III-V semiconductors exhibit strong optical nonlinearity. For instance, the third-order nonlinear susceptibility of passive InGaAsP/InP waveguides is $|\chi^{(3)}| \approx 4.2 \times 10^{-10}$ esu at the telecom wavelength [24]. On the

other hand, the Kerr coefficient of silicon at the telecom wavelength is $n_2 \approx 4.2 \times 10^{-14}$ cm^2/W [25], and the resulting value of $|\chi^{(3)}|$, estimated from the equation [26]

$$n_2(\text{cm}^2/\text{W}) = 0.0395 \times |\chi^{(3)}|(\text{esu})/n_0^2, \tag{1.1}$$

where n_0 is the refractive index of the material, is around $\approx 1.1^{-11}$ esu. A comparison between the two materials shows that the third-order susceptibility of InGaAsP/InP is about an order of magnitude higher compared to that of silicon. The ternary compound AlGaAs, which has been shown to be a promising material for nonlinear optics, has the Kerr coefficient of $n_2 \approx 1.5 \times 10^{-13}$ cm^2/W [19], resulting in $|\chi^{(3)}| \approx 4.1 \times 10^{-11}$ esu, a few times greater than that of silicon. In such a way, we can expect the optical nonlinearity of other III-V semiconductors to be relatively high.

Strong nonlinearities usually come along with undesirable effects such as nonlinear absorption. In ternary and quaternary compounds, one has a good control over this characteristic. One can change the bandgap wavelength over a wide range of values merely by adjusting the composition of the material. By shifting the bandgap wavelength, one can shift the edge of linear and two-photon absorption to a different wavelength region. Therefore, it is possible to minimize the losses due to linear and nonlinear absorption for a wavelength of interest. Overall, these benefits of III-V semiconductors justify our effort at studying their nonlinear optical properties which largely lack data in literature.

1.3 Applications of III-V Semiconductors

III-V semiconductors are in the basis of nearly every optoelectronic device in optical communications. The use of this class of materials have drawn attentions since the invention of light-emitting diodes (LEDs). The discovery of minority carrier injections

and the invention of transistors led to foundation of LEDs and laser diodes [27, 28], which, along side with the important role of III-V semiconductor compounds in optoelectronic, opened the path for today's more sophisticated III-V photonic integrated circuits (PICs). As an example, today, InP-based PICs can fulfill almost all required functions for optical transmitters and receivers. They are widely fabricated and used in optical communication industry in the scale of hundreds of elements on-a-chip [29].

III-V semiconductors are made up of many materials with unique electronic and optical properties. These properties can be modified by applying different techniques of material growth along with flexibility in design, such as in refractive index, bandgap or thickness of the material. The ability to tune the material bandgap energy, *i.e.* bandgap wavelength, have opened up the way to many present-day commercial devices, such as lasers, modulators, detectors, attenuators, (de)multiplexers, and a variety of waveguides. Different applications can be considered for III-V semiconductor chips. In this section, we will review the most important ones.

The first application is III-V device technologies for high-speed electronics and optics. For instance, heterojunction bipolar transistors, and heterostructure field-effect transistors, which are mostly based on GaAs and InP substrates, are used for ultra-high-speed electronics. On the other hand, commercially available optical modulators based on III-V semiconductors have shown the modulation capability of up to 40 Gb/s [30].

The second application widely using semiconductor devices is fiber optics networks. Optical communications rely on integrated lasers, modulators, amplifiers and switches which are used for transmitting and receiving optical signals through fibers. InGaAsP lattice matched to InP can be suitable for long fiber communications because of its low loss and low dispersion in the lowest-loss window of the optical fiber. Additionally, this material supports longer-wavelength (*i.e.*, L-band) operation in

optical fibers [31].

The third example is solid-state lightning applications. Many III-V-based LEDs are used for power signaling. One particular particular characteristic material is GaN used for blue and green LEDs, and also implemented for ultra-violet short-wavelength emitting [32, 33].

Last, but not least, is the optical storage application. Laser diodes are used to write on all of the common optical storage discs (CD, DVD, and Blu-ray). The shorter is the wavelength of the laser, the more dense is writing, and the more data can be stored in the discs. DVDs use red light (the wavelength of 650 nm), while CDs use 780 nm (infrared light). Blu-ray discs, on the other hand, use shorter wavelengths of 405 nm (violet) to store more data, thus demonstrating much more capacity compared to other discs. Generally, III-V compounds GaAs, GaN, and AlGaInP are used for this application [34, 35].

1.4 Objectives

The work reported herein extends prior efforts to find a suitable material platform that can handle a variety of functions in order to perform all-optical signal processing. From the literature discussed in Section 1.2, the benefits of III-V semiconductor compounds over other materials are apparent. However, among all III-V semiconductor compounds, a comprehensive study on nonlinear optical properties of quaternary III-V semiconductors is largely missing in literature. This research studies promising quaternary III-V compounds for nonlinear optics in four steps: identifying the suitable quaternary materials, designing waveguides based on them, wafer growth and fabrication, and performing optical characterization on the waveguides.

The procedure of identifying suitable quaternary materials includes detecting a material which provides wide range of refractive indices. Such material also needs to

avoid linear and nonlinear losses in operational wavelengths. Based on the two above mentioned criteria, aluminium gallium arsenide antimonide (AlGaAsSb) and indium gallium arsenide phosphide (InGaAsP) are selected. The details of this process are discussed in Section 2.3.

The waveguide design analysis aims fulfilling four criteria, which are lattice-matching condition, single-mode operation of the waveguide, minimization of the effective mode area, and dispersion management. The purpose of this analysis is to design passive nonlinear waveguides which are capable of demonstrating efficient nonlinear effects. An example of efficient nonlinear effect is four-wave mixing, which is a key process in many all-optical signal processing operations.

The wafer growth was done by Canadian Microelectronics Corporation (CMC) and the fabrication was processed at Cornell NanoScale Science & Technology Facility (CNF) at Cornell University and Quantum NanoFab Facility (QNF) at the University of Waterloo. Due to time constrains of my M. Sc. program, the fabrication was undertaken by Kashif M. Awan, the PhD candidate of Nonlinear Photonics group at the University of Ottawa.

In the last step, the optical characterization on the waveguides are conducted in order to assess the efficiency of the material. For the purpose of this thesis, the optical characterization has been only performed for InGaAsP/InP waveguides due to time constrains.

1.5 Outline of the Thesis

Chapter 2 of the thesis describes the crucial criteria for material selection and considered factors in waveguide design. In Chapter 3, we present the detailed design and modal analysis of AlGaAsSb and InGaAsP optical waveguides. The wafer growth and fabrication procedure of the waveguides are briefly reviewed in Chapter 4. Chapter

5 summarizes the experimental results and linear and nonlinear characterization of InGaAsP waveguides. Chapter 6 gives an example of one of the most generic building-blocks used in photonic integrated circuits for transmitters and receivers in optical fiber communication systems. In particular, we describe our work on the tolerance analysis of a spot-size converter based on InP technology. Following that, a summary, conclusions and future work are given in Chapter 7.

Chapter 2

Material Selection and Design Criteria

The work discussed in this chapter consists of the following main parts: overview of some of the important optical properties of III-V semiconductor compounds, principle of operation of waveguides, material selection, and waveguide design criteria. At the end of the chapter, we provide a background for the relevant nonlinear optical effects. The discussion of these topics is a prerequisite for waveguide design, which is discussed in Chapter 3.

2.1 Overview of Optical Propertie of III-V Semiconductors

In order to be able to identify promising material candidates for nonlinear photonic devices, it is important to geather the information about optical properties of different representatives of III-V semiconductor material group. The review in this section consists of important information about the band-gap energies and other optical

properties as functions of alloy composition for different III-V ternary and quaternary semiconductor compounds.

In Table 2.1, we present experimental values of some characteristics of several III-V compounds latticed-match to their substrates (as specified next to each compound). As an example of use of Table 2.1, let us consider $In_xGa_{1-x}As_yP_{1-y}$ semiconductor compound. The table indicates that it is lattice-matched to InP, and it has a direct bandgap with the energy E_0 between 0.75 and 1.35 eV. The specific value of the bandgap energy is dictated by the molar fraction y of As as it varies from 0 to 1. The corresponding minimum and maximum values of the refractive index n are also given for these molar fractions. The lattice matching will be discussed later in this chapter. Any of the materials shown in Table 2.1 can potentially have applications for a specific wavelength range, as dictated by its bandgap energy.

In Table 2.2, we summarize some of the III-V semiconductor compounds and specify the corresponding ranges of their bandgap wavelengths that a material can have for different compositions. With the help of this table, one can select a material based on its properties for a specific range of wavelengths. For example, the compound AlGaAsSb/GaSb, in the range of its compositions, can have bandgap wavelengths in all the telecom optical wavelength bands. In another example, when it is desirable to avoid two-photon absorption in the wavelength above 2 μm, a material that has a bandgap wavelength smaller than 1 μm can be selected.

Table 2.1: Properties of different III-V semiconductor compounds

Material	Substrate	x	y	Bandgap Type*	$E_0(eV)$	$\lambda(\mu m)$	$n^{**}_{\min}$	$n^{**}_{\max}$	ref
$Al_xGa_{1-x}As_ySb_{1-y}$	GaSb	0	0	D	0.72	1.72	3.72	3.90	[36]
		1	0.08	I	2.24	0.55	3.20	5.49	
	InP	0	0.51	D	0.77	1.61	3.55	3.78	
		1	0.56	I	2.39	0.51	3.06	4.88	[37]
	InAs	0	0.08	D	0.68	1.82	3.69	3.87	
		1	0.16	I	2.23	0.55	3.18	5.38	
$Ga_xIn_{1-x}P_yAs_{1-y}$	GaAs	1	0	D	1.43	0.86			[36]
		0.51	1	D	1.91	0.64	3.43	3.66	
	InP	0.46	0	D	0.75	1.65	3.11	3.59	
		0	1	D	1.35	0.91			
$Ga_xIn_{1-x}As_ySb_{1-y}$	GaSb	0	0.91	D	0.28	4.42	3.47	3.68	[36]
		1	0	D	0.72	1.72	3.72	3.89	
	InP	0.47	1	D	0.71	1.74			
		1	0.51	D	0.77	1.61			[37]
	InAs	0	1	D	0.36	3.44	3.42	3.66	
		1	0.08	D	0.66	1.87	3.69	3.87	
$Al_xGa_yIn_{1-x-y}P^{\dagger}$	GaAs	0	0.51	D	1.90	0.65	3.13	3.78	[36]
		0.53	0	I	2.33	0.53	2.92	3.75	
$Al_xGa_yIn_{1-x-y}As^{\ddagger}$	InP	0	0.46	D	0.75	1.65	3.42	3.66	[36]
		0.48	0	D	1.49	0.83	3.17	3.87	
$InP_xAs_ySb_{1-x-y}$	InAs	0.69	0	D	0.51	2.43	3.39	3.79	[37]
		0	1	D	0.36	3.44	3.42	3.65	
$Al_xGa_{1-x}Sb$		0	-	D	0.72	1.72	3.8	4.28	[36]
		1	-	I	2.27	0.54	3.13	3.37	
GaP_xAs_{1-x}		0	-	D	1.43	0.86	3.32	3.58	[36]
		1	-	I	2.76	0.45	3.02	3.51	
$Al_xGa_{1-x}As$	GaAs	0	-	D	1.43	0.86	3.41	3.72	[36]
		1	-	I	3.01	0.41	2.88	4.18	
$Ga_xIn_{1-x}P$	GaAs	0	-	D	1.35	0.91	3.05	4.54	[36]
		1	-	I	2.76	0.45			
		0.51	-	D					
$Ga_xIn_{1-x}Sb$	GaSb	0	-	D	0.17	7.29	3.95	5.13	[36]
		1	-	D	0.72	1.72	3.71	5.33	
$Ga_xIn_{1-x}As$		0	-	D	0.35	3.54	3.64	4.51	[36]
		1	-	D	1.43	0.86			
		0.47	-	D					
$c-Al_xGa_{1-x}N^{\star}$		0	-	D	3.23	0.38	2.35	2.77	[36]
		1	-	D	5.2	0.23	2.04	2.27	
$w-Al_xGa_{1-x}N^{\star}$		0	-	D	3.42	0.36			[36]
		1	-	D	6.2	0.2			
$w-Al_xIn_{1-x}N^{\star}$	GaN	0	-	D	0.7	1.77	2.14	2.73	[38]
		1	-	D	6.2	0.2			
		0.5	-	D					

* D=Direct band gap. I=Indirect bandgap.

** $n_{\min}$ is minimum refractive index, and $n_{\max}$ is maximum refractive index found in literature

† The refractive index value is shown for $(Al_xGa_{1-x})_{0.53}In_{0.47}P$/GaAs.

‡ The refractive index value is shown for $(Al_xGa_{1-x})_{0.48}In_{0.52}P$/InP.

⋆ The $c-$ symbol indicates the crystal structure is Cubic. The $w-$ symbol indicates the crystal structure is Wurtzite.

2.2 Optical Waveguides

An optical waveguide is a structure used for guiding light in a similar manner like metal wires guide electric charges. An optical waveguide is a building block of any photonic integrated circuit (PIC): it is used to guide light between its different components; moreover, it is a key building block of any integrated optical component itself. In principle, a waveguide limits a spatial region for light to propagate through. The key elements of waveguides are a dielectric medium with high refractive index, called a *core* or *guiding layer*, surrounded by materials with lower refractive indices, known as *claddings*. Most of practical waveguide structures exhibit two-dimensional confinement, which means that the light expansion in two dimensions is limited, and the third dimension serves as the propagation direction. The light is then guided by the mechanism of total internal reflection. Basically, there are two classical representations of waveguiding: the geometrical (ray) optics, and wave optics.

In geometrical optics, the propagation of light can be described using Snell's law, illustrated in Figure 2.1. Let us consider a beam of light traversing the boundary between two media with different refractive indices, n_1 and n_2. According to the Snell's law, the relationship between the angles of incidence and refraction with respect to the normal to the interface between the two media, θ_i and θ_t, is

$$n_1 \sin(\theta_i) = n_2 \sin(\theta_t). \tag{2.1}$$

If the refractive index of the medium of incidence n_1 is greater than that of the medium of refraction n_2, at a certain value of the angle of incidence of light onto the interface, the angle of refraction can reach 90 degrees, so that there is no beam refracted into the second medium. This angle of incidence is called *critical angle*. All the beams with the angles of incidence greater than the critical angle ($\theta_i > \theta_c$) experience total internal reflection at the boundary between the two interfaces.

Table 2.2: Bandgap wavelength ranges of several III-V semiconductor compounds

Material	Substrate	λ<1(μm)	O-band 1.26 - 1.36 μm	E-band 1.36 -1.46 μm	S-band 1.46 - 1.530 μm	C-band 1.53 - 1.565 μm	L-band 1.565 - 1.625 μm	U-band 1.625 - 1.7 μm	λ>1.7(μm)
$Al_xGa_{1-x}As_ySb_{1-y}$	GaSb	*	*	*	*	*	*	*	
	InP	*	*	*	*	*	*		*
	InAs	*	*	*	*	*	*	*	
$Ga_xIn_{1-x}P_yAs_{1-y}$	GaAs	*	*	*	*	*	*	*	
	InP	*							
$Ga_xIn_{1-x}As_ySb_{1-y}$	GaSb								*
	InP						*	*	*
	InAs								*
$Al_xGa_yIn_{1-x-y}P$	GaAs	*							
$Al_xGa_yIn_{1-x-y}As$	InP	*	*	*	*	*	*	*	
$InP_xAs_ySb_{1-x-y}$	InAs								*
$Al_xGa_{1-x}Sb$		*	*	*	*	*	*	*	*
GaP_xAs_{1-x}		*							
$Al_xGa_{1-x}As$	GaAs	*							
$Ga_xIn_{1-x}P$	GaAs	*							
$Ga_xIn_{1-x}Sb$	GaSb								*
$Ga_xIn_{1-x}As$		*	*	*	*	*	*	*	*
$c-Al_xGa_{1-x}N$		*							
$w-Al_xGa_{1-x}N$		*							
$w-Al_xIn_{1-x}N$	GaN	*	*	*	*	*	*	*	*

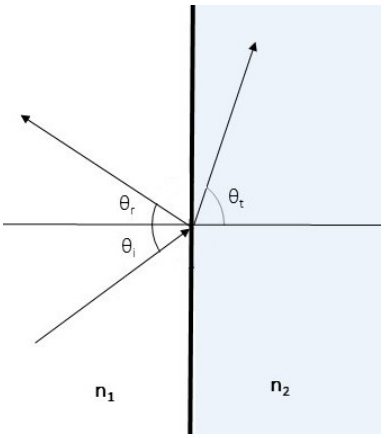

Figure 2.1: Demonstration of the Snell's law.

This effect is in the basis of waveguiding. In order to guide a beam light in a waveguide, a layer of higher-refractive-index material should be sandwiched between two layers of lower-refractive-index materials. Figure 2.2 shows such structure where n_1 and n_2 represents refractive indices of the core and cladding, respectively. The angle the guided wave makes with the normal to the interface between the core and claddings should satisfy the total internal reflection condition, *i.e.*, $\theta_i > \theta_c = \sin^{-1}(n_2/n_1)$.

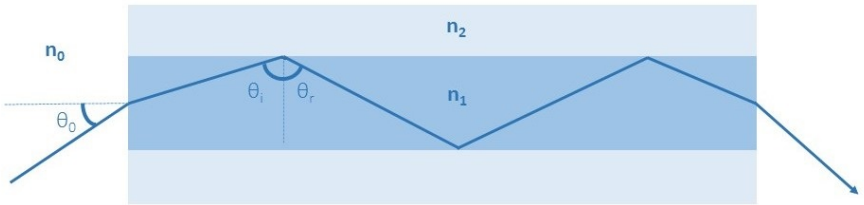

Figure 2.2: Incident beam undergoes total internal refraction at core-cladding interface. Incident beam is guided by the core only if the angle θ_0 is not too large.

Acceptance angle is the maximum angle of divergence of the light cone entering the waveguide core, such that all the light rays within the cone can experience total internal reflection in (can be guided by) the waveguide. In Figure 2.2, the acceptance angle is denoted by θ_0. It can be defined as

$$\theta_0 = \sin^{-1}\left(\frac{\sqrt{n_1^2 - n_2^2}}{n_0}\right), \tag{2.2}$$

in which n_1, n_2, n_0 are the refractive indices of the core, claddings, and the medium surrounding

the waveguide which is typically the air. The sine of the acceptance angle, $\sin\theta_0$, is known as the *numerical aperture*, and is determined by the refractive index contrast between the core and cladding.

Optical waveguides can be classified based on their geometries. The simplest form of a waveguide consists of a core sandwiched between the claddings made of the same lower-index material (symmetric slab dielectric waveguide). These waveguides confine the light mode in only one direction, thus exhibiting 1D guidance. The waveguides with 2D confinement can have different geometries such as rib, ridge, embedded strip, *etc.* Figure 2.3 shows different type of waveguides based on their geometries.

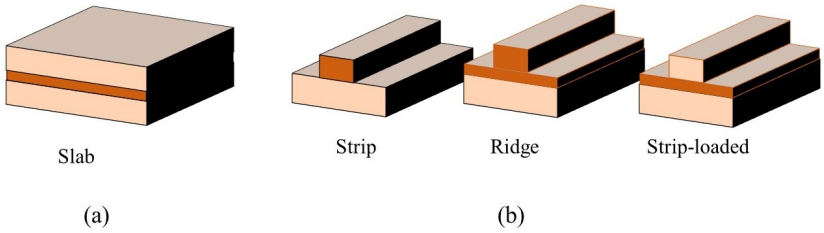

Figure 2.3: Different waveguide geometries. Darker shadings indicate higher refractive index.

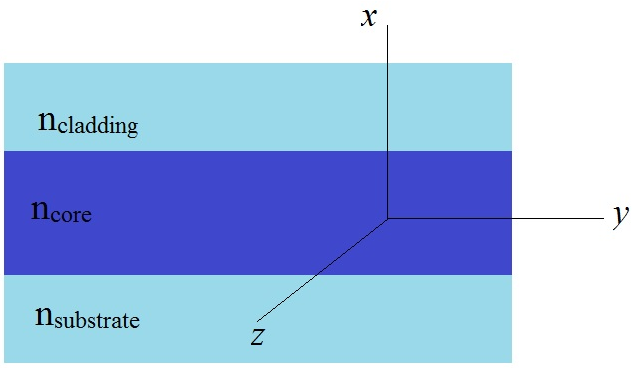

Figure 2.4: Schematic of a planar waveguide. A high-index core sandwiched between two lower index layers.

Geometrical optics shows that light can stay confined within the waveguide only for specific incident angles. Different angles correspond to different modes. However, when the thickness of the core is small, *i.e.*, on the scale of a wavelength, one has to resort to wave optics to understand the waveguiding mechanism. The underlying principles behind waveguiding in all types of waveguides are

similar. Since it is easier to illustrate these principles while considering a waveguide structure with 1D confinement, we evaluate guided-wave propagation in a simple slab dielectric waveguide. Consider a non-magnetic dielectric waveguide where the core layer is sandwiched between two lower-index layers, as depicted in Figure 2.4. In such a waveguide, an optical mode is the solution of Maxwell's equations with the appropriate boundary conditions. For monochromatic waves, modes can be obtained by solving curl equations driven from Maxwell's equations for dielectric materials [39]:

$$\begin{aligned} \nabla \times E &= i\omega\mu_0 H \\ \nabla \times H &= -i\omega\epsilon_0 n^2 E \end{aligned} \tag{2.3}$$

Waveguide modes can be found by solving these equations for each layer. The boundary conditions are tangential components of electric field and magnetic field being continuous at both interfaces. Thus, waveguide modes are obtained by applying boundary conditions in each layer of waveguide. Solving following equations will lead to optical modes:

$$\begin{aligned} \frac{\partial E_z}{\partial y} - \frac{\partial E_y}{\partial z} &= i\omega\mu_0 H_x, & \frac{\partial H_z}{\partial y} - \frac{\partial H_y}{\partial z} &= i\omega\epsilon_0 n^2 E_x \\ \frac{\partial E_y}{\partial x} - \frac{\partial E_x}{\partial y} &= i\omega\mu_0 H_z, & \frac{\partial H_y}{\partial x} - \frac{\partial H_x}{\partial y} &= i\omega\epsilon_0 n^2 E_z \\ \frac{\partial E_x}{\partial z} - \frac{\partial E_z}{\partial x} &= i\omega\mu_0 H_y, & \frac{\partial H_x}{\partial z} - \frac{\partial H_z}{\partial x} &= i\omega\epsilon_0 n^2 E_y \end{aligned} \tag{2.4}$$

These equations have two sets of polarized solutions: for Transverse Electric (TE) modes where E_z =0 and E_y =0, and for Transvers Magnetic (TM) modes where H_z =0 and H_y =0. The equations in 2.4 can be solved in each layer separately by using $n = n_{\text{core}} = n_{\text{cladding}} = n_{\text{substrate}}$. TE and TM modes propagation in a dielectric planar waveguide is schematically shown in Figure 2.5

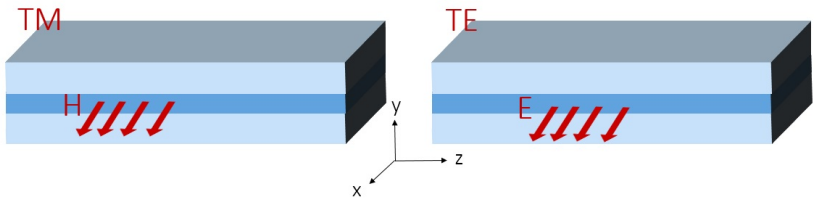

Figure 2.5: Propagation of TE and TM modes along axis z in a planar waveguide.

However, in most waveguides, the light confinement happens in two dimensions. The exact modes of such 2D waveguides cannot be computed easily as there are no pure TE or TM mode. All modes have some component of E and H in the direction of their propagation. Thus, one has

to consider vectorial Maxwell's equations where the scalar approximation does not hold anymore. That is why, the best and more precise method would be to resort to numerical simulations that can perform a precise modal analysis. For that reason, we use the commercial software *Lumerical Mode Solutions* to design our waveguide structures. In this work, we will be only focusing on two types of waveguides exhibiting 2D mode confinement, namely a *strip-loaded* waveguide and a *nanowire*. The specifics of these geometries will be provided later in this chapter.

2.3 Material Selection

As discussed earlier, one can have some control over the characteristics of a ternary or quaternary III-V semiconductor within some parameter space. The ternary compounds can be schematically represented as $A_xB_{1-x}C$, where A, B, and C can be replaced with the appropriate chemical elements specific to a compound. The parameter x is the mole fraction which can range from 0 to 1. The properties of such material can be modified by varying x. A quaternary semiconductor compound can be represented in a similar fashion as $A_xB_{1-x}C_yD_{1-y}$, where A and B are atoms from the column III, and C and D are atoms from the column V of the Periodic Table. A quaternary compound typically has two degrees of freedom as the mole fractions x and y of two pairs of elements can now be adjusted. Therefore, one can expect more flexibility in designing and selecting the optical properties of the resulting material.

In this work, we study two quaternary III-V semiconductor compounds: $Al_xGa_{1-x}As_ySb_{1-y}$ and $In_xGa_{1-x}As_yP_{1-y}$. These compounds are superpositions of several binary compounds. The binary compounds AlAs, GaAs, GaSb, and AlSb can be alloyed to form quaternary $Al_xGa_{1-x}As_ySb_{1-y}$ composition. $In_xGa_{1-x}As_yP_{1-y}$ is based on GaP, GaAs, InAs, and InP. The parameters x and y show the mole fractions of Al, Ga, As, and Sb in $Al_xGa_{1-x}As_ySb_{1-y}$, and of In, Ga, As, and P in $In_xGa_{1-x}As_yP_{1-y}$, respectively. The concentration of pairs of elements, represented by x and $1-x$, and by y and $1-y$, sum up to 1. One can change the properties of these quaternary materials by mutually adjusting the concentrations x and $1-x$, as well as y and $1-y$.

The dependencies of the lattice constant and energy gap on the material compositions of ternary and quaternary semicon- ductor compounds can be found from Vegard's law [40] which allows one to find an unknown parameter (lattice constant or bandgap energy) of a ternary (or quaternary) compound if the corresponding parameter for its constitutive binary alloys is known. According to Vegard's law, an unknown parameter T_{ABC} of a ternary semiconductor compound $A_xB_{1-x}C$ can be

interpolated based on the knowledge of its corresponding binary constituent parameters T_{AC} and T_{BC} and the mole fraction x as

$$T_{ABC}(x) = xT_{AC} + (1-x)T_{BC}. \tag{2.5}$$

Similarly, for a $A_xB_{1-x}C_yD_{1-y}$ quaternary compound, T_{ABCD} can be found from T_{AC}, T_{AD}, T_{BC}, T_{BD}, x, and y according to

$$T_{ABC}(x) = xyT_{AC} + x(1-y)T_{AD} + (1-x)yT_{BC} + (1-x)(1-y)T_{BD}. \tag{2.6}$$

In Figure 2.3, we display the lattice constants and bandgap energies of AlGaAsSb and InGaAsP for their different material compositions (different x and y). Each point on the graph represents a binary alloy. The lines connecting the points represent the interpolation of the corresponding parameters for ternary compounds, given by Eq. (2.1). For instance, the material AlGaAs is represented by the line connecting GaAs and AlAs in Figure 1. This line is nearly vertical, which means that various material compositions of $Al_xGa_{1-x}As$ (represented by different x) are lattice-matched (can be grown epitaxially on top of each other without tolerating much lattice strain). This is one of the reasons why AlGaAs is a popular material in photonic integrated circuits. The solid and dashed lines demonstrate direct and indirect-bandgap compounds. The areas bounded by the lines represent the corresponding parameters for quaternary materials. In this plot, areas bounded by the red and blue lines indicate $\mathrm{In_xGa_{1-x}As_yP_{1-y}}$ and $\mathrm{Al_xGa_{1-x}As_ySb_{1-y}}$ parameter space, respectively.

The values of lattice constants and bandgap energies of the binary alloys that were used to obtain the curves in Figure 2.3 are listed in Table 2.3. The binary alloys have zincblende crystalline structure, so do their corresponding quaternary compounds, $\mathrm{In_xGa_{1-x}As_yP_{1-y}}$ and $\mathrm{Al_xGa_{1-x}As_ySb_{1-y}}$. The parameters E_0 and E_g^X in Table 2.3 represent the energy gaps for the direct Γ-valley and indirect valley of the binary alloy, respectively. Different binary allows have their indirect minima either on either X or L valleys. For the binary alloys listed in Table 2.3, all the energy bandgaps of X-valley are smaller compared to those of L-valley. This is the reason why the indirect bandgap is represented by E_g^X, not by E_g^L.

The starting point in the design and fabrication of an integrated optical device based on ternary or quaternary III-V semiconductor is to define the material compositions of its substrate, upper and lower claddings, and the guiding layer. These layers should have nearly equal lattice constants which should also match the lattice constant of the substrate. If the substrate and the layers' compositions

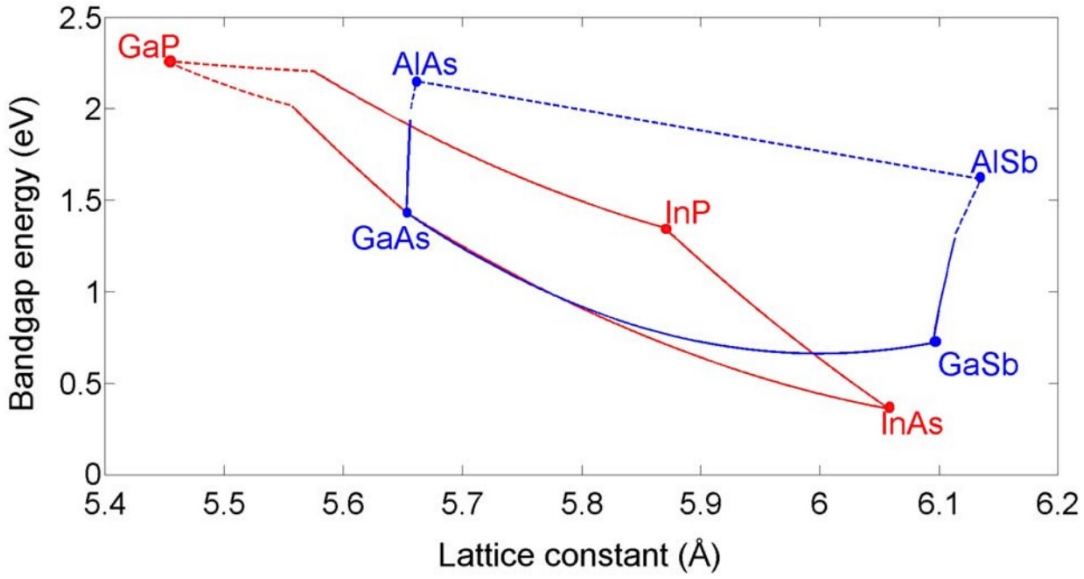

Figure 2.6: Lattice constant and band-gap energy for InGaAsP (red line) and AlGaAsSb (blue line) quaternary compounds. The lines represent the parameters for the ternary compounds, and the parameter space bounded by the red and blue lines correspond to InGaAsP and AlGaAsSb quaternary compounds, respectively. The solid and dashed lines display direct and indirect-bandgap compounds, respectively.

are selected properly, defect-free epitaxial growth of the layers on top of the substrate is possible. Otherwise, a lattice mismatch between the layers will lead to a poor-quality, high-defect-density epitaxial growth. Furthermore, even if the right compositions for a nearly perfect lattice matching are chosen, a lattice mismatch during the growth process can still occur because of other reasons, such as temperature variations of lattice parameters.

Table 2.3: Lattice constants and band-gap energies of binary alloys

Material	Lattice constant (Å)	E_0 (eV)	E_g^X (eV)
AlAs	5.661	3.01	2.15
AlSb	6.135	2.27	1.615
GaP	5.450	2.76	2.261
GaAs	5.653	1.43	1.911
GaSb	6.095	0.72	1.05
InP	5.869	1.35	2.21
InAs	6.058	0.359	1.37
InSb	6.479	0.17	1.63

One can refer to Figure 2.3 for finding a suitable substrate and lattice-matched layer arrangement. For example, in order to epitaxially grow an AlGaAsSb layered assembly, the options for a substrate can be AlAs, InP, InAs, and GaSb since all of them have their lattice constants within the parameter area corresponding to AlGaAsSb quaternary compound (bounded by blue lines). GaAs and AlSb cannot be substrate candidates for growing AlGaAsSb since there is no quaternary AlGaAsSb compositions that could match their lattice constants with those of these binary compounds. After selecting the substrate, one can then select the compositions of other layers. The corresponding lattice-matched compositions lie on a vertical line (parallel to the Y-axis of the graph), which passes through the point representing the selected substrate material. In this Master thesis work, GaAsb and InP are chosen as the substrates for AlGaAsSb and InGaAsP, respectively. As it can be seen from Figure 2.3, these binary alloys can be lattice-matched with corresponding quaternary compounds in a relatively wide range of parameters.

After selecting the substrate, the material compositions of different layers should be identified. There are two main factors to consider when selecting a material composition: the refractive index contrast that different layets can make with respect to each other, and the bandgap wavelength of the material. The refractive index of a quaternary compound depends on the mole fractions x and y. For maximum mode confinement in the waveguide, one needs to maximize the refractive index contrast between the guiding layer and claddings: $\Delta n = n_{\text{core}} - n_{\text{cladding}}$. Another important factor is related to bandgap wavelength. If the energy of a photon propagating through a semiconductor material is larger than its bandgap energy, the photon can get absorbed by the electrons residing at top of the valance band which can then get excited to the conduction band. Therefore, such light can experience a strong absorption loss in a semiconductor material with the bandgap energy smaller than the energy of the associated photons. Moreover, if the sum of the energies of two photons is high enough, they can simultaneously get absorbed by the electrons leading to their excitation to the conduction band. This nonlinear optical process is called two-photon absorption, and it can occur when the energy of the photon is greater than half of the semiconductor bandgap energy. To avoid both linear and two-photon absorptions, the semiconductor bandgap energy should be at least twice the photon energy, or in other words, the bandgap wavelength should be less than half of the photon wavelength [19].

In Table 2.4, we present the refractive indices and bandgap wavelengths for InP and GaSb, which are our selected substrates, and different compositions of $\mathrm{In_xGa_{1-x}As_yP_{1-y}}$ and $\mathrm{Al_xGa_{1-x}As_ySb_{1-y}}$ which present the maximum achievable refractive index contrasts. These compositions are lattice-

matched to their corresponding binary substrates. Looking at the table, one can see the wavelength boundaries within which $In_xGa_{1-x}As_yP_{1-y}$ and $Al_xGa_{1-x}As_ySb_{1-y}$ are lattice matched to InP and GaSb, respectively. This table provides the information about the parameter limits for a passive device operation. For instance, by looking at the table, one can find out that AlGaAsSb allows passive devices operating in telecommunication C-band since it can have bandgap wavelengths more than one half of the conventional telecom wavelength 1550 nm. This motivates us to select this material as a possible alternative to the well-studied AlGaAs. In contrast to $Al_xGa_{1-x}As$, $Al_xGa_{1-x}As_ySb_{1-y}$ has two mole fractions x and y to adjust, thus potentially offering more freedom in fine-tuning its optical properties such as refractive index. That is why, we believe that studying nonlinear optical performance of this material at the C-band telecommunication wavelength range is worthwhile. We have selected the compositions of claddings and core of our AlGaAsSb waveguides taking into consideration this choice of operation wavelengths.

At the same time, it can be seen from Table 2.4 that InGaAsP is not suitable for passive device operation in the Telecom C-band because of the characteristic values of its bandgap wavelengths. On the other hand, integrated passive InGaAsP waveguides can be used in combination with InGaAsP lasers in order to extend their operational wavelengths to 2000 nm and beyond. InGaAsP has many applications and can serve both as a laser source and a material for light detection. As an example, the InGaAsP/InP diode laser finds application as a tunable source for high-resolution laser spectroscopy in near- infrared spectral region. This sort of spectroscopy can be used in chemical and biological analysis [41, 42]. In addition, there has been much interest in mid-wavelength and long-wavelength infrared photodetection [43–45]. Complicated structures such as quantum well infrared photodetectors (QWIP) using lattice-matched InGaAsP/InP has been demonstrated in long-wavelength infrared detection and has been reported to be more efficient in 1.55 μm compared to AlGaAs/GaAs QWIPs [43]. It is possible to develop an integrated circuit with laser diodes and detectors co-integrated along with passive waveguides, using only quaternary InGaAsP based upon indium phosphide. This is an additional reason why studying the nonlinear optical performance of InGaAsP passive waveguides could be of practical value.

Table 2.4: Refractive index at 1550 nm and direct-bandgap wavelength of lattice-matched AlGaAsSb/GaSb and InGaAsP/InP.

	n	λ_g (nm)
$Al_{0.1}Ga_{0.9}As_{0.01}Sb_{0.99}$	3.85	1430
$AlAs_{0.08}Sb_{0.92}$	3.28	550
$In_{0.58}Ga_{0.43}As_{0.9}$ $P_{0.1}$	3.62	1250
InP	3.17	920
GaSb	3.98	1720

2.4 Dispersion

One of the factors that plays an important role in nonlinear optical interactions is group velocity dispersion (GVD). GVD entails the dependence of the group velocity of light passing through a medium on its wavelength. Let us assume that there are different pulses with different group velocities co-propagating through a nonlinear medium. Even if the pulses are launched at the medium at an exactly the same instant of time, they will lose their temporal overlap after propagating for distance due to the difference of their group velocities in the medium. This effect is called temporal walk-off, and it limits the efficiency of the nonlinear optical interaction between the medium and the two pulses [46]. GVD is responsible for the temporal walk-off between the wavelengths co-propagating through the optical waveguide. The larger the spectral difference between the interacting wavelengths, the shorter the distance they travel together before they separate. GVD can be defined as the derivative of the inverse group velocity with respect to the angular frequency, or, in other words, as the second derivative of the phase constant β with respect to the angular frequency:

$$\beta_2 = \frac{\partial}{\partial\omega}\frac{1}{\nu_g} = \frac{\partial}{\partial\omega}\left(\frac{\partial\beta}{\partial\omega}\right) = \frac{\partial^2\beta}{\partial\omega^2}. \tag{2.7}$$

Another important parameter characterizing the dispersion of light as it propagates through an optical waveguide is the dispersion parameter D that has two contributions. The first contribution to D is due to the fact that the refractive index of the material varies with optical frequency (or wavelength) which causes the group velocity to vary. This is referred to as material dispersion, and the associated dispersion parameters are fixed for a specific material. The second contribution, known as waveguide dispersion, involves the dependence of the propagating beam's group velocity on the waveguide geometry. The waveguide dispersion arises from the difference in the refractive indices and group velocities that the propagating wave "sees" as it passes through the core and

claddings. Optical waveguides with larger dimensions mostly exhibit the material dispersion; the waveguide dispersion in them is insignificant [7].

In a different limit in which the dimensions of the waveguide are relatively small compared to the wavelength of the guided light, the confinement of the light within the core becomes looser. The mode can then penetrate into the media surrounding the guiding layer (the claddings and air). In this case, both the material and waveguide contributions to the overall dispersion parameter D are of significance. When both the contributions are present, they are not necessarily additive, and can cancel the effect of each other. When the surrounding medium has the refractive index notably different from that of the guiding layer material, the waveguide dispersion can compensate, or even overcompensate the material dispersion [47]. This can result in zero-dispersion wavelength region that can significantly enhance the nonlinear interactions. In this case, the temporal walk-off become insignificant, and the spectral difference between the interacting beams that still results in efficient nonlinear optical interactions can become very large. This is mostly desirable for widely tunable nonlinear optical interactions, such as four-wave mixing.

In this study, we have performed a dispersion analysis for both InGaAsP/InP and AlGaAsSb/GaSb optical waveguides which will be discussed in Chapter 3.

2.5 Waveguide Design Criteria

In this section, we will evaluate and summarize the factors that one needs to take into consideration for designing a nonlinear passive waveguide. The aim is to design a waveguide, capable of demonstrating efficient nonlinear effects such as wavelength conversion, which plays a key role in all-optical networks. To secure efficient nonlinear optical interactions, first step is to maximize the efficient nonlinear coefficient, given by [48]:

$$\gamma = \frac{2\pi n_2}{\lambda A_{\text{eff}}}, \tag{2.8}$$

in which n_2 is the Kerr coefficient (nonlinear refractive index) of the waveguide, λ is the wavelength of light traveling through the waveguide, and A_{eff} is the effective mode area. A_{eff} is defined as

$$A_{\text{eff}} = \frac{\left[\int_{-\infty}^{\infty}\int_{-\infty}^{\infty} |E(x,\,y)|^2 \,\mathrm{d}x\,\mathrm{d}y\right]^2}{\int_{-\infty}^{\infty}\int_{-\infty}^{\infty} |E(x,\,y)|^4 \,\mathrm{d}x\,\mathrm{d}y} \tag{2.9}$$

where $E(x, y)$ is the electric field amplitude [16].A_{eff} depends on the waveguide parameters such as core-cladding index contrast and dimensions of the structure. It can vary from values less than 1 μm^2 to more than 10 μm^2, depending on the waveguide design. Below we summarize the criteria for designing a waveguide.

2.5.1 Lattice matching

As discussed earlier in this section, layers of different material compositions grown on top of each other epitaxially are chosen to match their lattice constants in order to minimize the film stress. In general, trying to grow layers of unmatched lattice constants on top of a substrate, cause strained or relaxed growth and lead to inter-facial tension. Such deviations can cause changes in the optical and electrical properties of the film. In practice, it is almost impossible to have a perfectly matched lattices. However, in many applications, nearly matched lattices are desirable to minimize the defects.

If the lattice mismatch between the substrate and the film grown on top of the substrate is large, the film material needs to strain to accommodate the lattice structure of substrate. If the thickness of film exceeds a critical value, the dislocation defects at the interface will form a relaxed epitaxy and the film layer returns to its initial lattice-structure above the interface [49]. Figure 2.7 shows the schematic of a strained, relaxed, and lattice-matched structure.

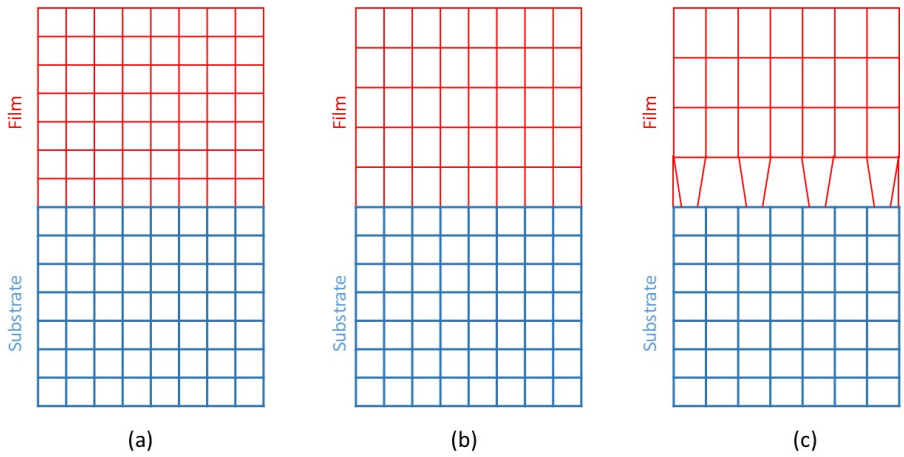

Figure 2.7: Figure shows the growth of a film over a substrate while the epitaxy is (a) lattice-matched, (b) strained, and (c) relaxed.

The lattice mismatch is typically defined by $\Delta a/a$, wheer a is the lattice constant and Δa is the difference between the lattice constants of the film and substrate. $\Delta a/a$ of 0.06% for the growth of $In_{0.53}Ga_{0.47}As$ on InP substrate using liquid-phase epitaxy has been reported [50]. This value is reported to be $\Delta a/a \approx 0.4\%$ [51] for the growth of InGaAsP on InP using supercooling technique. A similar study done for the growth of AlGaAsSb on top of GaSb shows a lattice mismatch of 0.13% [52]. The reported values for lattice mismatch are relatively small, resulting in low-defect-density epilayers. Hence, these semiconductor compounds can be suitable for photonics applications.

2.5.2 Wavelength range of operation

While adjusting the composition for matching the lattices of layers, one should also consider the bandgap energy of the guiding layer (corresponding to the lattice-matched composition). The criterion for the band-gap wavelength of a semiconductor material requires that the photon energy of the light should be below the half band-gap energy of the material. In such way, it is possible to decrease the effect of two-photon absorption.

Two-photon absorption is usually a significant problem in the design of all-optical devices. If the energy difference between lower and upper states of the atom is equal or less than sum of the energies of two photons, an electron residing at valance band can absorb the photons in the process of two-photon absorption and traverse the bandgap. At low intensities, this absorption is much weaker than linear absorption (including only one photon). However, since this nonlinear process depends on the square of intensity, it can dominate over the linear absorption at high intensities. A schematic of this process is shown in figure 2.8(a). Two-photon absorption can be completely eliminated by using a material in which the lowest energy level stays more than $2hv$ above the ground state, as shown in figure 2.8(b).

2.5.3 Minimization of the effective mode area

In general, one of the terms used to judge the strength of nonlinearity of a device, is effective mode area. One of the outcomes of a small effective mode area is that the optical intensity for a given power level becomes high. In this case, nonlinearities become significant. Also, smaller mode areas indicate strong guiding of the mode in the waveguide core. However, in some applications, using optical fibers with large mode area is more desirable because in such fibers the optical intensity in not high enough to cause any significant nonlinearities, thus increasing the optical reach of such

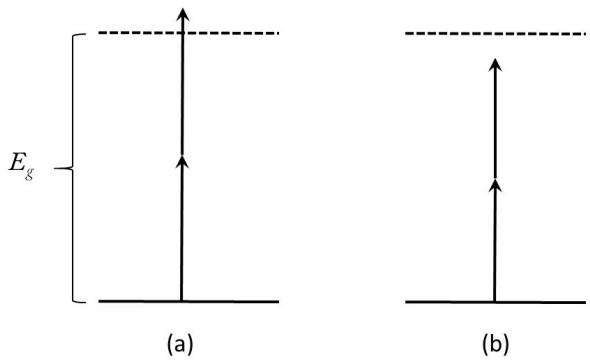

Figure 2.8: (a) Two-photon absorption process. (b) Two-photon absorption can be eliminated when the laser frequency lies below half-band-gap of the material.

fiber communication system and increasing the optical power value for the damage threshold. Some of these fibers are a matter of interest for high-power applications such as amplification of intense optical pulses [53, 54].

Referring to Equation 2.8, one can conclude that it is possible to maximize the nonlinear coefficient by minimizing the effective mode area. There are different ways to minimize A_{eff}. One can increase the refractive index contrast between core and claddings by picking up suitable compositions of the epilayers, in accordance with the values within the range of lattice matching and bandgap energy requirements. Furthermore, one can design the waveguide geometry and pick its dimensions in order to obtain the effective mode area as small as possible.

As mentioned above, one can maximize the waveguide nonlinear coefficient by minimizing the effective mode area. The effective mode area is the smallest for the fundamental mode. That is the reason why one has to ensure that the designed waveguide is single-mode, guiding only the fundamental TE and/or TM modes.

2.5.4 Dispersion management

Dispersion management is a term used for tailoring and engineering the dispersion properties of a device to enhance some particular functions. As discussed earlier, this can be done through properly selecting a material or choosing suitable dimensions of the waveguide. One of the possibilities of dispersion management is dispersion compensation. It is possible to cancel out different forms of dispersion in a waveguide to produce zero GVD frequencies. The importance of this matter can be seen in various nonlinear effects such as four-wave mixing (FWM) [55].

Let us consider the FWM effect in its simplest form, where the frequencies of the two pump photons are the same, *i.e.*, ω_p=ω_{p1}=ω_{p2}. There is also a signal wave which has the frequency ω_s different from that of the pump. The interaction between these three photons (with the frequencies ω_{p1}, ω_{p2}, and ω_s) gives rise to the fourth photon, known as the idler photon with the frequency ω_i. The value ω_s dictates the frequency of the generated idler beam ω_i by the relationship $2\omega_p$=ω_s+ω_i. This interaction is schematically shown in Figure 2.9.

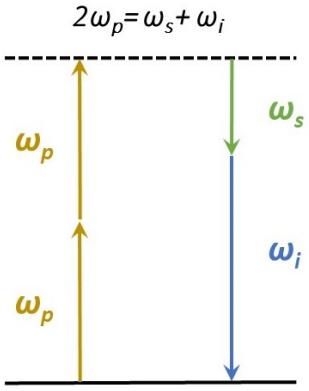

Figure 2.9: Simple form of four-wave mixing process.

It is desirable to enhance the spectral distance between signal and idler waves in order to have more efficient four-wave mixing. This can be done by matching the operational wavelength ω_p with the zero-GVD wavelength. Therefore, we will have near-zero dispersion at wavelengths around ω_p and the material see the same dispersion and index at frequencies ω_s and ω_i. It is possible to achieve zero GVD point at wavelength of interest by dispersion engineering, which is feasible in waveguides with sub-wavelength dimensions.

2.6 Studied Waveguides

In this study, we propose two designs of passive optical waveguides in both AlGaAsSb and InGaAsP. One hase relatively large dimensions and provides mainly material dispersion. In such a waveguide, a strip of the guiding layer (core) is confined between the claddings. This waveguide is referred to as *strip-loaded waveguide*. The reason why we are interested in strip-loaded structures is that the modes are well confined in the guiding layer and they do not sense much of fabrication imperfections or the epitaxial defects in the wafer growth and etching processes. Thus, the propagation loss is

expected to be much lower for these waveguides. For example, the propagation loss reported for AlGaAs strip-loaded waveguides is $\sim 1-3$ dB/cm [7].

The other design is a deeply-etched waveguide with sub-micron dimensions, referred to as *nanowires*. The propagation losses of the nanowires are expected to be much higher [16, 47, 56]. It can arise from different sources such as substrate leakage, exposure of optical mode to the side-wall roughness, or epitaxial defects. The propagation losses reported for AlGaAs nano wires are around $\sim 6-10$ dB/cm [16]. However, the dispersion management is possible in nanowires, which leads to efficient nonlinear optical interactions and widely tunable FWM. Moreover, very small effective mode area (less than 1 μm^2) can be achieved in nanowires which will strongly enhance the nonlinearity of the waveguide. A schematic of strip-loaded and nanowire waveguides can be seen in Figure 2.10.

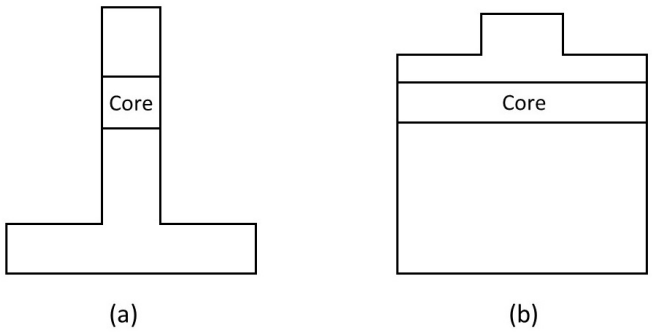

Figure 2.10: Types of studied waveguides: (a) nanowire and (b) strip-loaded.

2.7 Nonlinear optical effects

Nonlinear optical effects occur as a result of the nonlinear interaction of high-intensity light with a medium that it passes through. These effects are considered as "nonlinear" since they occur when the material's response to an optical field depends in a nonlinear manner on the amplitude of the optical field. The nonlinear response of the material can be observed when the applied optical field has sufficiently high intensity. At low intensities, the linear response dominates over the nonlinearity, so, the latter one cannot be observed.

To have a better and more accurate perspective, consider the relationship between the polarization of a material $\tilde{P}(t)$ and the strength of an applied optical field $\tilde{E}$(t). In the case if the input

field has a low intensity, this relation can be described linearly as [26]

$$\tilde{P}(t) = \epsilon_0 \chi^{(1)} \tilde{E}(t), \tag{2.10}$$

where the constant $\chi^{(1)}$ is the linear susceptibility of the material, and ϵ_0 is the permittivity of free space. However, in a nonlinear regime, where the applied intensity is sufficiently high, this response can be described as a Taylor series expansion of the polarization $\tilde{P}(t)$ with the field strength $\tilde{E}(t)$:

$$\tilde{P}(t) = \epsilon_0[\chi^{(1)}\tilde{E}(t) + \chi^{(2)}\tilde{E}^2(t) + \chi^{(3)}\tilde{E}^3(t) + \chi^{(4)}\tilde{E}^4(t) + ...]. \tag{2.11}$$

The $\chi^{(n)}$ is referred to as $n-th$ order nonlinear optical susceptibility of the medium. Consequently, we refer to $\tilde{P}^{(n)}(t) = \epsilon_0 \chi^{(n)} \tilde{E}^n(t)$ as n^{th}-order nonlinear polarization, which can be related to a particular nonlinear optical process. The physical processes that occur due to a second-order nonlinear polarization $\tilde{P}^{(2)}$ are likely to be different from those happen as a result of a third-order nonlinear polarization $\tilde{P}^{(3)}$. For example, the second-order susceptibility $\chi^{(2)}$ is responsible for three-wave mixing processes such a second-harmonic generation (SHG), difference-frequency generation (DFG), or sum-frequency generation (SFG) [5]. On the other hand, the third-order susceptibility $\chi^{(3)}$ is responsible for effects such a four-wave mixing (FWM) and self-phase modulation (SPM), which occur as a result of the intensity-dependent refractive index of the material. We discuss some of nonlinear optical effects that are of importance for the present study in following sections.

2.7.1 Self-Phase Modulation

Self-phase modulation (SPM) is a nonlinear optical process whereby an intensive beam of light propagating through a medium changes the propagation conditions to itself through interacting with the medium nonlinearly. This effect is accompanied by an intensity-dependent variation of the refractive index of the medium which is called *optical Kerr effect*. This variation causes a phase shift in the optical beam, resulting in the changes of the beam's spectral shape.

The intensity-dependent variation of the refractive index can be described as

$$n(t) = n_0(t) + n_2 I, \tag{2.12}$$

where n_0 is the linear refractive index, n_2 is the nonlinear refractive index, often referred to as the

Kerr coefficient, and I represents the optical intensity. The nonlinear phase shift acquired by the optical beam propagating through a medium is given by

$$\phi_{\mathrm{NL}}(t) = n_2 k_0 L I, \tag{2.13}$$

where $k_0 = 2\pi/\lambda$, and L is the length of the medium. As a result of the time-dependent phase change, the spectrum of the transmitted beam will be modified and might undergo changes (*e.g.*, most typically, broadening) compared to that of the incident beam. Figure 2.11 shows schematically the SPM process.

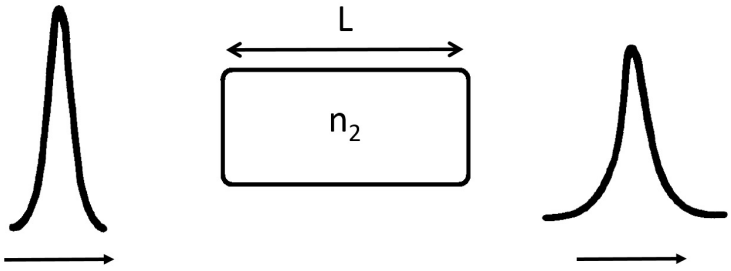

Figure 2.11: Self-phase modulation (SPM).

SPM has many applications such as optical switching [57] and spectral supercontinuum generation [58]. In general, the Kerr nonlinearity has been beneficial for different optical signal processing methods such as wavelength conversion.

2.7.2 Four-Wave Mixing

Four-wave mixing (FWM) is a nonlinear phenomenon that appears as a consequence of the third-order optical nonlinearity. In this effect, two or three different frequency components propagating through a nonlinear medium generate new frequency components. This nonlinear process is parametric [59], meaning that the conservation of energy holds between the participating photons. Assume that there are three input optical beams with three distinct frequencies ω_1, ω_2, and ω_3, entering the material and interacting with it. The nonlinear variation of the refractive index results in the four-wave mixing effect accompanied by the generation of a new frequency ω_4 ($\omega_1 + \omega_2 - \omega_3 = \omega_4$). This process is called *non-degenerate four-wave mixing* because all four frequency components participating in the process are different. Figure 2.12 illustrates non-degenerate four-wave mixing process.

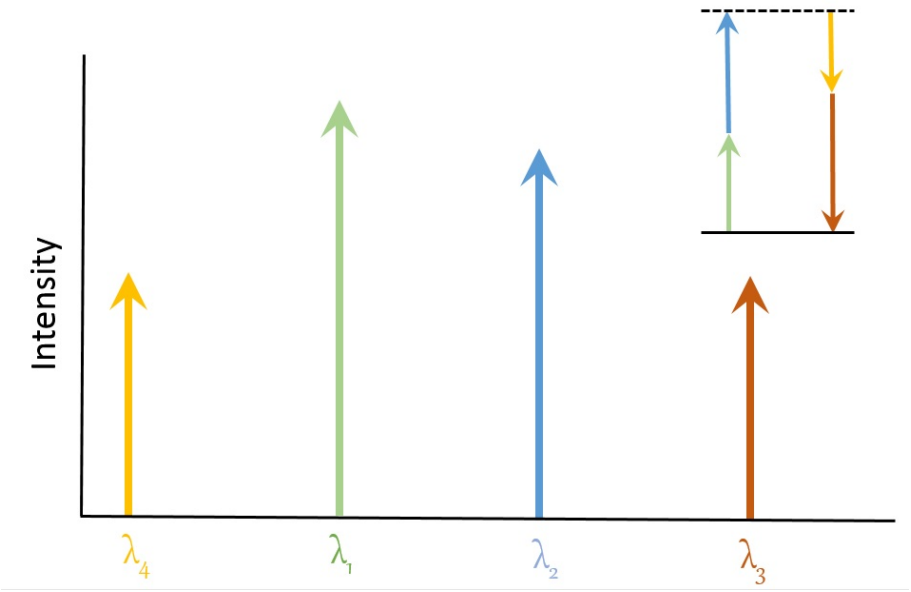

Figure 2.12: Generation of new wavelengths via non-degenerate four-wave mixing.

A *degenerate four-wave mixing* can also occur, where the frequencies of two input photons are identical, such that there is a single *pump* beam donating two photons for each act of four-wave mixing, and a *signal* input frequency component distinct from the pump frequency. Two photons are taken away from pump: one for amplifying the *signal* wave, and one for generating a new *idler* frequency on the other side of the spectrum. A degenerate four-wave mixing in an optical waveguide is demonstrated in Figure 2.13. The frequency of the generated *idler* photon can be described as follow:

$$\omega_{\text{idler}} = 2\omega_{\text{pump}} - \omega_{\text{signal}} \tag{2.14}$$

FWM is a phase-sensitive process. To obtain an efficient FWM, there should be nearly zero mismatch between the relative phases of the interacting beams. One can minimize the phase mismatch by matching the *pump* wavelength with a zero-dispersion wavelength. FWM can find applications in phase conjugation [60], supercontinuum generation [61], optical image processing and holographic imaging [62] in addition to all-optical signal processing application targeted by the present study.

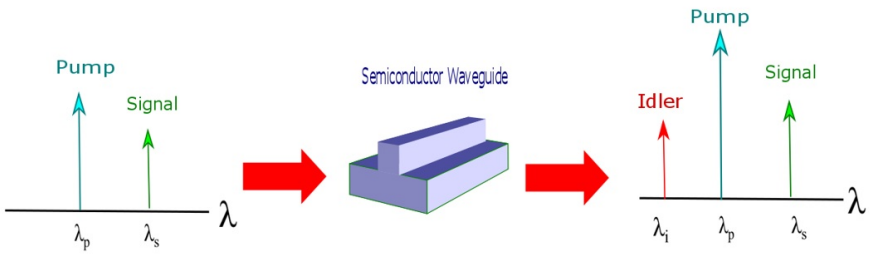

Figure 2.13: Degenerate four-wave mixing in a nonlinear optical waveguide.

Chapter 3

Waveguide Design

In this chapter, we will present waveguide designs, including their geometries and compositions, for both AlGaAsSb and InGaAsP. Here we discuss two types of waveguides with different geometries. One type is strip-loaded waveguide, which is a strip of a higher-refractive index core confined between cladding layers with an index difference to form the guiding channel. In such a waveguide, the core layer is not etched throug, and the upper cladding is etched partly. The second waveguide geometry is called nanowire made of the guiding layer confined between cladding layers, all three of which are etched through. The nanowire can have waveguide widths much narrower compared to those of the strip-loaded waveguides. The two waveguide geometries are compared through simulations in this chapter.

3.1 AlGaAsSb Waveguides

AlGaAsSb multilayer III-V semiconductor wafers can be grown via metalorganic chemical vapor deposition (MOCVD), or by molecular beam epitaxy (MBE). The first method entails gas phase transform of the material which will be deposited on the substrate. The deposition will eventually occur via a chemical reaction on the substrate. MBE can be an alternative to MOCVD. It is an epitaxy method for thin-film deposition of crystals. It takes place in specific chambers under high temperatures to ensure a fully dust-free environment. In general, MBE is a more common way to grow III-V wafers, and this technique has been used for the growth of our wafers. The wafer growth and fabrication processes will be discussed in next chapter.

As discussed earlier, the lattice matching of different layers can be achieved by choosing a proper composition of a pair of elements in the quaternary compound. Following the mentioned criteria, a suitable material composition was selected for the core and cladding layers. The substrate GaSb was chosen for both the waveguide designs which are the strip-loaded waveguides and the nanowires, and the rest of the layers were chosen for each waveguide geometry to be lattice-matched to substrate. Once the lattice-matched compositions were determined, the dimensions of the waveguides were selected in a way to minimize the effective mode area for the fundamental TE and TM modes. For this purpose, we used a commercial mode solver *Lumerical MODE Solutions*, and modified the waveguide parameters while tracking the value of the effective mode area. In the following sections, we discuss the waveguide designs for both strip-loaded waveguide and the nanowire.

3.1.1 AlGaAsSb nanowire

Figure 3.1 represents the structure of AlGaAsSb nanowire waveguide along with its dimensions and material composition. The guiding layer is chosen to have the composition of 60% of aluminum since its bandgap energy is large enough to avoid both the linear and nonlinear absorption at the wavelength 1550 nm. The corresponding refractive index is 3.52 at $\lambda = 1550$ nm. In order to have a large refractive index contrast with the guiding layer, we chose the compositions of the claddings to be $Al_{0.82}Ga_{0.18}As_{0.07}Sb_{0.93}$. The refractive index associated with this composition is 3.29, which leads to the index contrast of $\Delta n = 0.23$. On the other hand, the substrate material GaSb has the refractive index of 3.98 which is much larger than the refractive index of the core. This could lead to a mode leakage into the substrate, and to the loss of guidance. To avoid this situation, the thickness of the lower cladding was chosen to be 3 μm, which is large enough in order to prevent the mode leakage to the substrate. For the simulations, the etch depth of the waveguides was fixed at 1.2 μm, so that the mode confinement at the core is strong and there is no mode leackage to the high-index substrate. By the etch depth, we mean the height from the top of upper cladding layer down to where the etching stops. The widths of the nanowires varied between 200 and 1200 nm. In this range, we expect a strong mode confinement and single-mode operation. Table 3.1 represents the summary of the structural and material parameters of the waveguides.

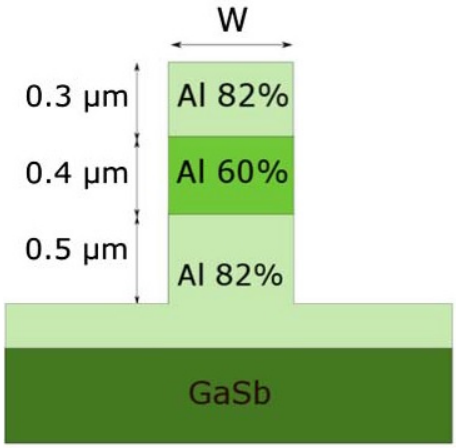

Figure 3.1: The structure of the designed nanowire. The compositions of the upper cladding, the guiding layer, and the lower cladding are $Al_{0.82}Ga_{0.18}As_{0.07}Sb_{0.93}$, $Al_{0.6}Ga_{0.4}As_{0.05}Sb_{0.95}$, and $Al_{0.82}Ga_{0.18}As_{0.07}Sb_{0.93}$, respectively. "W" denotes the width of waveguide.

Table 3.1: Material parameters and layer thicknesses of AlGaAsSb wafer for nanowires

	Composition	Thickness (nm)	E_g (eV)	λ_g (nm)	n
Upper cladding	$Al_{0.82}Ga_{0.18}As_{0.07}Sb_{0.93}$	300	1.95	636	3.29
Guiding layer	$Al_{0.6}Ga_{0.4}As_{0.05}Sb_{0.95}$	400	1.61	770	3.52
Lower cladding	$Al_{0.82}Ga_{0.18}As_{0.07}Sb_{0.93}$	3000	1.95	636	3.29
Substrate	GaSb		0.72	1722	3.98

In Figure 3.2, we show the intensity distribution for the fundamental TE and TM mode in nanowire. In the simulation, the waveguide width is fixed at 700 nm. The effective mode areas achieved for TE and TM modes are 0.33 and 0.41 μm^2, respectively. These small values ($\ll 1\ \mu m^2$) promise of a good nonlinear optical performance.

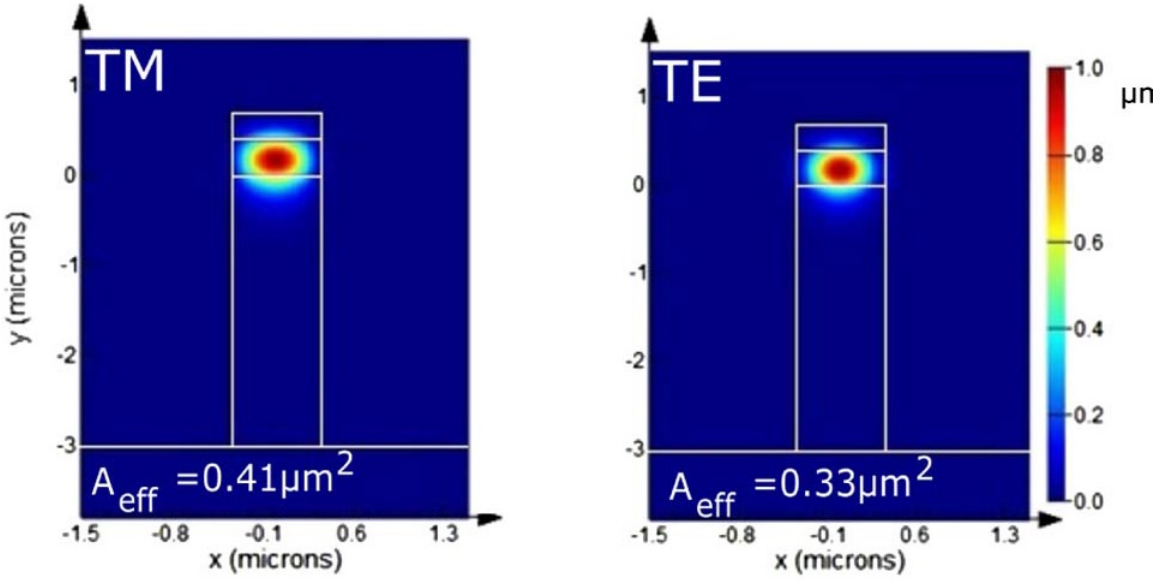

Figure 3.2: Intensity distributions of the fundamental TE and TM modes in AlGaAsSb nanowire with the width of $w = 700$ nm. The effective mode areas of the TM and TE modes are 0.41 μm^2 and 0.33 μm^2 for the nanowires, respectively.

3.1.2 AlGaAsSb strip-loaded waveguides

Figure 3.3 shows the structure of the designed strip-loaded waveguides. These waveguides have larger dimensions, and they are thus expected to have lower propagation loss compared to that of the nanowires. Similarly to the nanowires, the composition of the guiding layer was chosen to be $Al_{0.6}Ga_{0.4}As_{0.05}Sb_{0.95}$ to make sure that the bandgap energy is large enough to avoiding linear and nonlinear absorption while still having a high index contrast with the claddings. The composition of the upper and lower claddings are $Al_{0.66}Ga_{0.34}As_{0.06}Sb_{0.94}$ and $Al_{0.82}Ga_{0.18}As_{0.07}Sb_{0.93}$, respectively. The corresponding refractive indices are 3.48 for the upper cladding, and 3.29 for the lower cladding. This leads to the index contrast of $\Delta n = 0.04$ between the core and upper cladding, and $\Delta n = 0.23$ between the core and lower cladding. The reason for the small index contrast between the core and upper cladding is to obtain a more circular mode profile. It is expected to increase

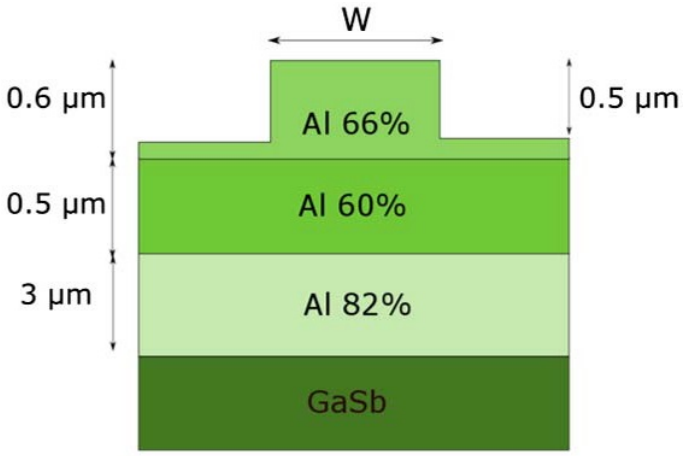

Figure 3.3: The structure of the designed strip-loaded waveguide. The compositions of the upper cladding, the guiding layer, and the lower cladding are $Al_{0.66}Ga_{0.34}As_{0.06}Sb_{0.94}$, $Al_{0.6}Ga_{0.4}As_{0.05}Sb_{0.95}$, and $Al_{0.82}Ga_{0.18}As_{0.07}Sb_{0.93}$, respectively.

the efficiency of coupling between the waveguide and the beam from free-space or the optical fiber by a minimization of the mode shape mismatch. On the other hand, the relatively high refractive index contrast between the core and the lower cladding could help one to achieve a stronger mode confinement, and hence, to prevent the mode leakage into substrate. Also, the thickness of the lower cladding is sufficiently large (3 μm) to avoid the mode leakage. In the simulations, the etch depth of the waveguide was fixed at 0.5 μm, while the widths vary from 600 to 1600 nm. Table 3.2 shows the important parameters for AlGaAsSb strip-loaded waveguides.

Figure 3.4 shows the intensity distribution of fundamental TE and TM modes for AlGaAsSb strip-loaded waveguide. The corresponding values of the effective mode areas are 1.4 and 1.13 μm^2 for TE and TM mode, respectively. To the best of our knowledge, these values are much smaller than any effective mode area reported for a strip-loaded III-V semiconductor waveguide. Thus, we can expect to see more efficient nonlinear optical performance with our improved designs.

3.1.3 Simulations and Results

We carried out a modal analysis of the fundamental TE and TM modes for both the strip-loaded waveguides and the nanowires with the widths ranging between 200 and 1200 nm for strip-loaded waveguides, and 600 to 1600 nm for the nanowires. Figure 3.5(a) shows the effective mode area as a function of the waveguide width for a fixed wavelength of $\lambda = 1550$ nm. One can clearly see

Table 3.2: Material parameters and layer thicknesses of AlGaAsSb wafer for strip-loaded waveguides

	Composition	Thickness (nm)	E_g (eV)	λ_g (nm)	n
Upper cladding	$Al_{0.66}Ga_{0.34}As_{0.06}Sb_{0.94}$	600	1.71	725	3.48
Guiding layer	$Al_{0.6}Ga_{0.4}As_{0.05}Sb_{0.95}$	500	1.61	770	3.52
Lower cladding	$Al_{0.82}Ga_{0.18}As_{0.07}Sb_{0.93}$	3000	1.95	636	3.29
Substrate	GaSb		0.72	1722	3.98

two regimes on the graph. In the first regime, the effective mode area increases monotonically with the waveguide width. This regime corresponds to the waveguide widths of 300 nm and above for the fundamental TE mode, and 200 nm and larger for the fundamental TM mode. In this regime, the mode is well confined within the guiding layer. In the second regime, where the widths of the waveguide are less than 300 nm for the TE and 200 nm for the TM modes, a different trend can be observed. The effective mode area increases with the decrease of the waveguide width. The reason to this behaviour is that the waveguide width becomes so small that the fundamental mode gradually approaches its cut-off, thus loosing its confinement in the core and spreading to the surrounding regions. This regime is also referred to as the *cutoff regime*. This trend is more observable for the TE mode since this mode is more dependent on the waveguide width. The minimum effective mode area around $\sim 0.2\,\mu m^2$ was achiever for the nanowires with the widths around 300 nm.

In Figure 3.5(b), we plot the effective mode area for the fundamental TE and TM modes of an AlGaAsSb strip-loaded waveguide as a function of the waveguide width at the fixed value of the wavelength $\lambda = 1550$ nm. One can also distinguish the cutoff regime in this graph; however, it is not as pronounced as that of the nanowires. Our modal analysis indicates that the smallest effective mode area around $1.2\,\mu m^2$ in a strip-loaded waveguide can be achieved for the fundamental TM mode at the waveguide width 900 nm. For the fundamental TE mode, the minimum effective mode area $\sim 1.4\,\mu m^2$ corresponds to the waveguide widths between 1100 and 1200 nm. Since we intend to minimize the propagation loss by using relatively larger dimensions, 1100 nm seems to be a more

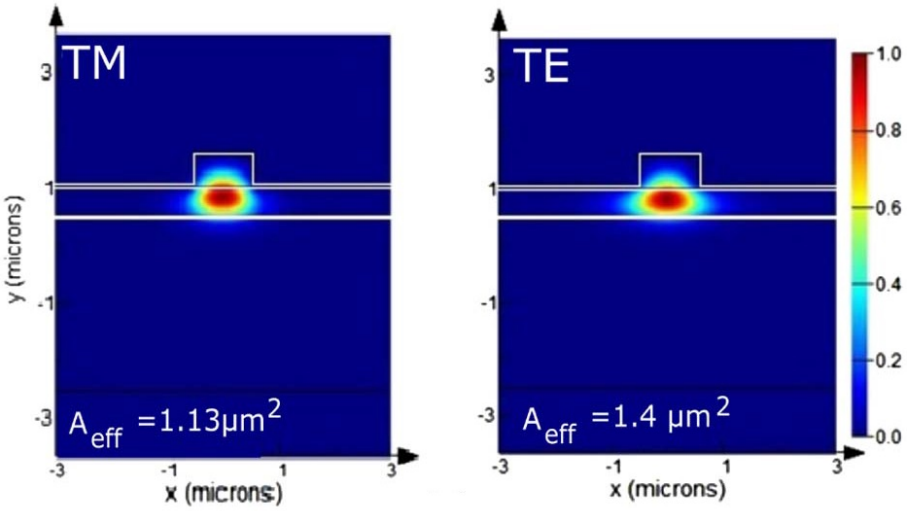

Figure 3.4: Intensity distributions of the fundamental TE and TM modes in AlGaAsSb strip-loaded waveguide with the width of $w = 1100$ nm. The effective mode areas of the TM and TE modes are 1.13 μm^2 and 1.4 μm^2, respectively.

suitable choice for the width of the designed strip-loaded waveguides.

To carry out the dispersion analysis, we used the method of second-order polynomial interpolation to perform the curve fitting of the GVD data points obtained from *Lumerical Mode Solutions*. In order to evaluate the accuracy of interpolation results, a statistic parameter coefficient called *the coefficient of determination*, also known as R^2, is used [63]: the higher is the value of R^2, the better is the fit. The values of R^2 in our studies were greater than 90% for each curve, indicating a good agreement between the data and the fitted curves.

In Figures 3.6 and 3.7, we present the dispersion analysis for both types of waveguides. Figure 3.6 shows the GVD dependencies on the wavelength for the fundamental TE [part (a)] and TM [part (b)] modes of a nanowire, respectively. We can see that it is possible to set the zero dispersion point for TE polarization at 1550 nm by varying the waveguide width. The wavelength corresponding to zero GVD point increases with the increase of the waveguide width. However, in the case of TM polarization, GVD values are larger and positive, which means there is no potential for dispersion management.

Figure 3.7 represent GVD dependencies for the fundamental TE [part (a)] and TM [part (b)] modes of a strip-loaded waveguide. Zero dispersion cannot be achieved in strip-loaded waveguides because the material dispersion in these structures is dominant. Therefore, GVD values are more positive and large for both the TE and TM polarizations.

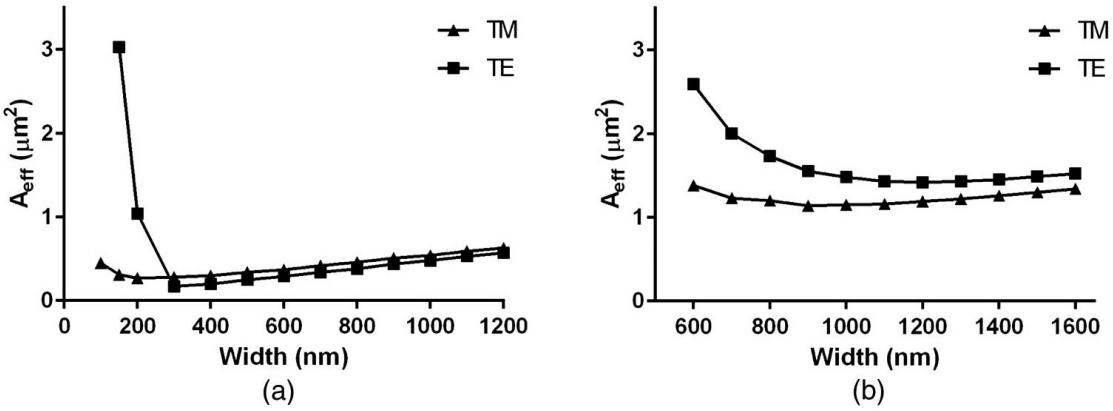

Figure 3.5: Effective mode area as a function of waveguide width at the wavelength 1550 nm for (a) AlGaAsSb nanowire, and (b) AlGaAsSb strip-loaded waveguide. The rectangular and triangular points represent the fundamental TE and TM modes, respectively.

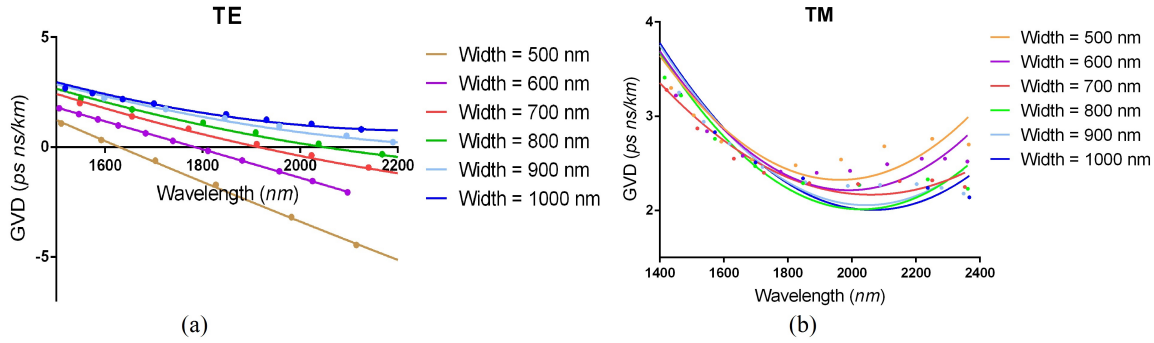

Figure 3.6: GVD as a function of wavelength for different values of AlGaAsSb nanowire widths: (a) for the fundamental TE mode, (b) for the fundamental TM modes. Solid lines show the data fit.

3.2 InGaAsP Waveguides

In this section, we present the design of InGaAsP nanowires and strip-loaded waveguides suitable for wide-range wavelength conversion. Ultimately, this kind of waveguides can be monolithically co-integrated with InGaAsP laser sources to extend their operation ranges to the wavelengths 2 μm and longer. In the following sections, we will discuss the design of InGaAsP nanowires and strip-loaded waveguides.

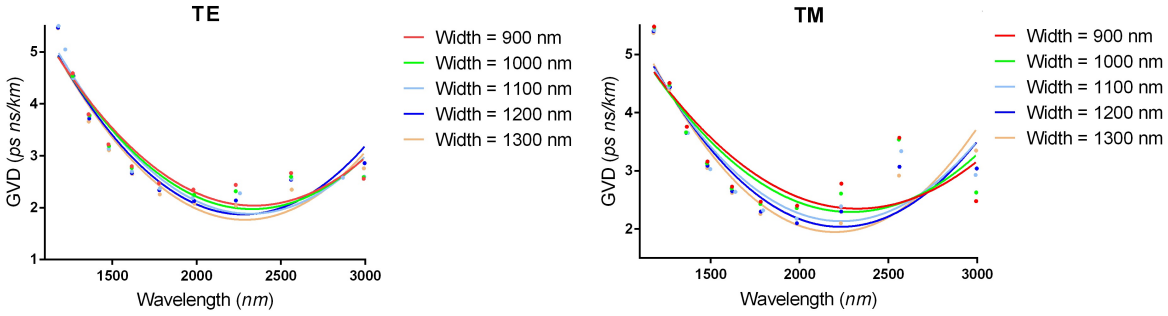

(a) (b)

Figure 3.7: GVD as a function of wavelength for different values of AlGaAsSb strip-loaded waveguide width: (a)for the fundamental TE mode, (b) for the fundamental TM mode. Solid lines show the data fit.

3.2.1 InGaAsP Nanowires

Figure 3.8 shows the waveguide geometry [part (a)] and the evolution of the fundamental TE mode as a function of wavelength [part (b)] in an InGaAsP nanowire. All the parameters, including the waveguide dimensions and the material compositions, are selected in accordance with the criteria described in Chapter 2. We were able to demonstrate guided modes in the range of wavelength between 1550 and 2750 nm.

As illustrated in Figure 3.8(a), the guiding layer was chosen to have 63% of indium to minimize the linear and nonlinear absorption at large wavelengths (around 3 μm). Due to the range of the badngap energies of various InGaAsP compositions, some two-photon absorption in telecom c-band will always be present. The cladding material was chosen to be InP so that we have a high refractive index contrast with the core for better mode confinement. The refractive index of the core is 3.58 at wavelength $\lambda = 1550$ nm and 3.37 at $\lambda = 2750$ nm. The refractive index of InP claddings is 3.17 at $\lambda = 1550$ nm and 3.11 at $\lambda = 2750$ nm. This yields the refractive index contrast of $\Delta n = 0.41$ at $\lambda = 1550$ nm, and $\Delta n = 0.26$ at $\lambda = 2750$ nm. In order to minimize the required etch depth during the fabrication process, the thickness of the upper cladding was set to 0.3 μm. The ultimated required etch depth for the nanowires was 2 μm. Figure 3.8(b) shows the intensity distribution of the fundamental TE mode for a 800-nm-wide waveguide at different wavelengths. As it can be seen from the figure, the mode expands as the wavelength increases. The calculation of the effective mode area indicates that A_{eff} changes from 0.38 to 0.7 μm^2 for the fundamental TE and from 0.43 to 0.85 μm^2 for the fundamental TM modes while the wavelength varies from 1550 to 2750 nm.

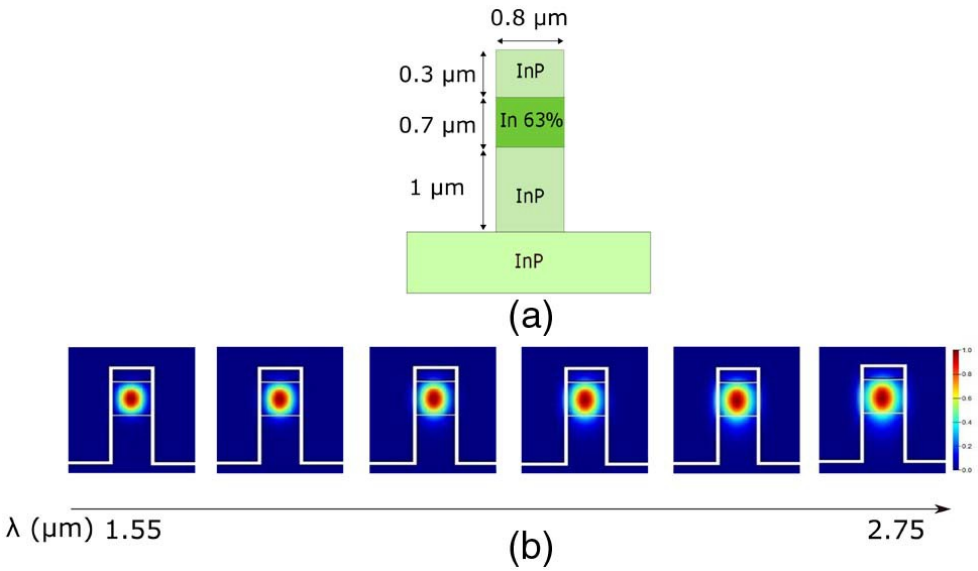

Figure 3.8: (a) Schematic of the designed InGaAsP nanowire with InP claddings and the composition of the guiding layer $In_{0.63}Ga_{0.37}As_{0.8}P_{0.2}$. (b) Intensity distributions of the fundamental TE mode of an InGaAsP nanowire with the width of $w = 800$ nm at different wavelengths. The evolution of the fundamental TE mode is shown as the wavelength increases from 1550 to 2750 nm.

Table 3.3 shows a summary of structural and material parameters of an InGaAsP nanowire.

3.2.2 InGaAsP Strip-Loaded Waveguides

The material composition of InGaAsP strip-loaded waveguides was selected to be the same as for the nanowires in order to maximize the refractive index contrast between the core and claddings while minimizing the linear and nonlinear absorptions. In Figure 3.9(a), we illustrate the schematic of the designed strip-loaded waveguide. The thickness of the guiding layer was set to 0.4 μm in order to minimize the effective mode area. The etch-depth of the strip-loaded waveguide was fixed at 0.9 μm. In figure 3.9(b), we show the evolution of the guided fundamental TE mode as the wavelength spans from 1550 to 2750 nm, for a waveguide with the width of 1.7 μm. The effective mode area calculations have shown that A_{eff} varied from 1.79 to 4.49 μm^2 for the fundamental TE mode, and from 1.03 to 4.34 μm^2 for the fundamental TM mode as the wavelength was changed from 1550 to 2750 nm. Table 3.4 shows the summary of the material and structural parameters of an InGaAsP strip-loaded waveguide.

Table 3.3: Material parameters and layer thicknesses of InGaAsP wafer for nanowires

	Composition	Thickness (nm)	E_g (eV)	λ_g (nm)	n
Upper cladding	InP	300	1.34	925	3.17
Guiding layer	$In_{0.63}Ga_{0.37}As_{0.8}P_{0.2}$	700	0.85	1459	3.58
Lower cladding	InP	1000	1.34	925	3.17
Substrate	InP		1.34	925	3.17

3.2.3 Simulations and Results

In Figure 3.10, we plot the effective mode area for the fundamental TE and TM modes as a function of wavelength for (a) an InGaAsP nanowire, and (b) an InGaAsP strip-loaded waveguide. As it can be seen from the figure, the effective mode area in both types of waveguides increases with wavelength. The fundamental TM mode in InGaAsP nanowires experiences a more significant increase with the wavelength compared to that of the fundamental TE mode as the TM mode has a weaker confinement in such waveguides.

The group velocity dispersion of InGaAsP waveguides with different widths is shown in Figure 3.11. The GVD as a function of wavelength for the fundamental TE and TM modes of InGaAsP nanowires is shown in Figures 3.11(a) and (b), respectively. It can be seen that from the graph that the TE mode in the nanowires has zero-dispersion points in the wavelength range between 1700 and 2300 nm. The GVD as a function of wavelength for the fundamental TE and TM modes in strip-loaded waveguides is shown in Figures 3.11(c) and (d), respectively. One can see from the figure that GVD for these waveguides can be reduced significantly compared to its material value, although it remains nonzero for this geometry. The relatively high R^2 values of more than 0.85 indicate a good agreement between the curves of Figure 3.11, and the data points obtained from *Lumerical* solutions.

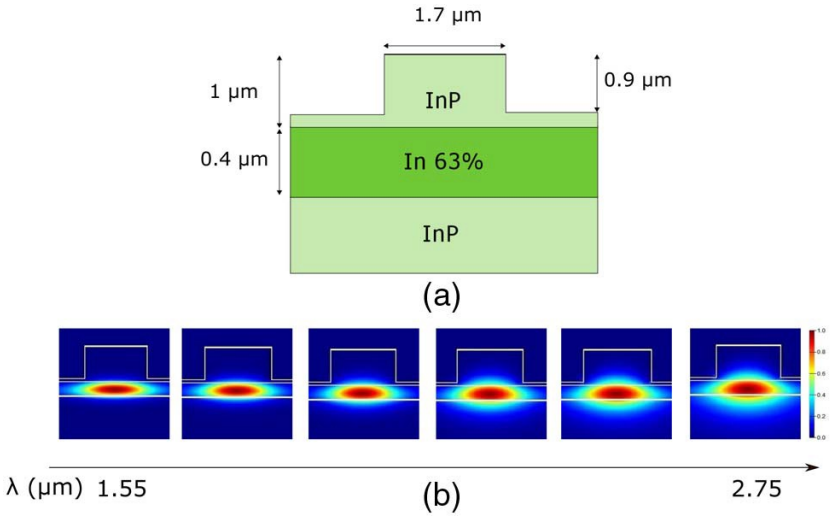

Figure 3.9: (a) Schematic of the designed InGaAsP strip-loaded waveguide with InP claddings and the composition of the guiding layer $In_{0.63}Ga_{0.37}As_{0.8}P_{0.2}$. (b) Intensity distribution of the fundamental TE mode of an InGaAsP strip-loaded waveguide with the width of w= 1700 nm at different wavelengths. The evolution of the fundamental TE mode is shown as the wavelength increases from 1550 to 2750 nm.

Table 3.4: Material parameters and layer thicknesses of InGaAsP wafer for strip-loaded waveguides

	Composition	Thickness (nm)	E_g (eV)	λ_g (nm)	n
Upper cladding	InP	1000	1.34	925	3.17
Guiding layer	$In_{0.63}Ga_{0.37}As_{0.8}P_{0.2}$	400	0.85	1459	3.58
Lower cladding	InP	1000	1.34	925	3.17
Substrate	InP		1.34	925	3.17

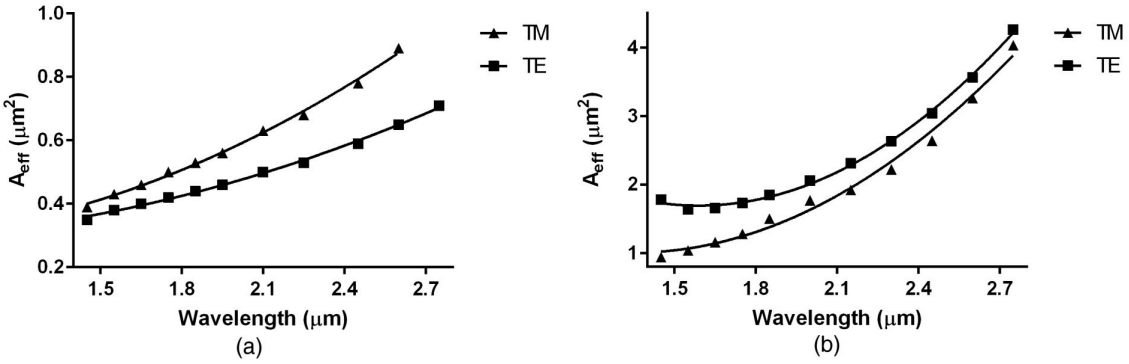

Figure 3.10: Effective mode area as a function of wavelength: (a) for an InGaAsP nanowire with the width 800 nm, (b) for an InGaAsP strip-loaded waveguide with the width 1700 nm. The rectangular and triangular points represent the simulated values of the effective mode area for the fundamental TE and TM modes, respectively. The solid line is the quadratic interpolation of the data.

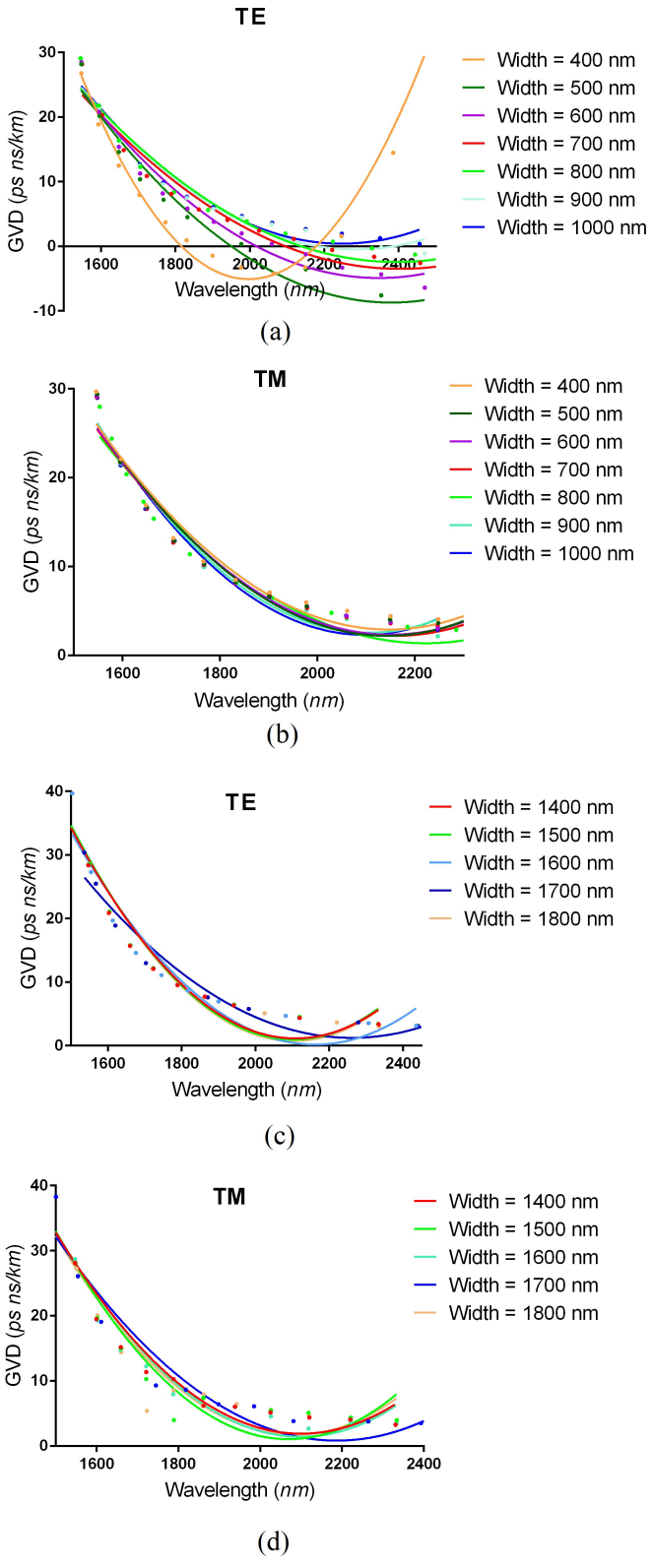

Figure 3.11: GVD as a function of wavelength for different values of InGaAsP waveguide widths as specified in the legend: (a), (b) for the fundamental TE and TM modes in a nanowire, and (c), (d) for the fundamental TE and TM modes in a strip-loaded waveguide, respectively. Solid lines indicate the fit.

Chapter 4

Fabrication of InGaAsP/InP Strip-loaded Waveguides

In the previous chapters, we proposed the measurements of the nonlinear optical responce of InGaAsP and AlGaAsSb passive optical waveguides. AlGaAsSb has the potentials of applications in optical communication networks, while InGaAsP optical waveguides can potentially extend the operation range of the common InGaAsP laser sources to the longer wavelengths. In Chapter 3, we have presented several waveguide designs based on these materials, together with the modal and dispersion analysis. The next step is to develop the fabrication process for high-quality and low-defect-density integrated optical waveguides based on these materials, and then to experimentally measure their nonlinear optical properties.

At this stage of the project, all four wafers for the four waveguide structures, two based on InGaAsP and two based on AlGaAsSb, have been grown. The wafer for InGaAsP nanowires was grown via molecular beam epitaxy (MBE), and the rest of the wafers, namely: the AlGaAsSb wafers and InGaAsP wafer for strip-loaded waveguides, have been grown via metalorganic chemical vapour deposition (MOCVD). Due to the time constrains of my M.A.Sc. program, so far, we have only performed experiments with InGaAsP strip-loaded waveguides. We thus focus mostly on the fabrication process of these structures in this chapter. The fabrication was undertaken by Kashif M. Awan, a Ph.D. candidate working under Drs. Dolgaleva's and Boyd's supervision.

4.1 Fabrication Process

4.1.1 Wafer Growth

The first step in the waveguide fabrication process is the growth of a vertically layered structure called *wafer*. There are two conventional methods of growing III-V semiconductor wafers: metalorganic chemical vapour deposition (MOCVD), and molecular beam epitaxy (MBE).

In MOCVD process, one can grow layers by depositing thin layers of atoms on a semiconductor substrate. The thickness of each layer can be controlled to obtain a material with a specific optical, thermal or electrical properties. The principle of MOCVD is as follows: the atoms supposed to be added in crystal are combined with organic gas molecules and passed over a hot semiconductor wafer. The heat splits the molecules and deposits demanded atoms on the semiconductor surface. This process is repeated layer-by-layer, and the lattice structures of these layers are perfectly aligned with the semiconductor substrate. The most common organometallic precursors used for the growth of InGaAsP on InP substrates are Trimethylindium (TMIn), Trimethylgallium (TMGa), Phosphine (PH3), and Tertiarybutyl phosphine (TBP). MOCVD takes place in cold wall reactors where many chemical reactions happen both in the vapor phase and at the growing surface. The MOCVD growth process can fall into four regimes: a reactant input regime where the chemical sources are used; a reactant mixing regime where the adduct and elimination reactions lead to a formation of polymer; a boundary layer regime above the substrate where the diffusion to the substrate and heating lead to pyrolysis; and finally the epitaxial growth on the substrate surface [64]. Since these processes may involve toxic gases, the growth chambers are very high-quality and expensive.

MBE is an epitaxy method for thin-film deposition of crystals. This process takes place in ultra-high vacuum (UHV) chambers, under high temperatures. Using the UHV chambers not only will result in a complete dust-free environment, but guarantees material purity. In this process, like MOCVD, the starting point is the base semiconductor material referred as the substrate. After heating the substrate to hundreds of degrees, precise beams of molecules are fired to the surface of the substrate from guns known as effusion cells. The molecules land on the surface, condense and build up the thin-layers gradually, and eventually form the crystal.

From the commercial and technical perspective, there has always been a debate which technology works better. However, for certain applications, the specific requirements define the superiority of a technique. For instance, MOCVD has more flexibility for sources and the reactor configuration can be modified, while MBE has less setup variability. One the other hand, MBE has a higher cost of the

material growth. MOCVD can process many wafers simultaneously, while MBE involves the growth of a single wafer. MOCVD is relatively fast while MBE is a very slow process [65]. Also, MBE is more precise compared to MOCVD in terms of controlling the thickness of each layer [66]. In our project, the InGaAsP epitaxial layers were grown via MOCVD on InP substrate. In the following subsection, we describe the steps of the fabrication process of InGaAsP strip-loaded waveguides.

4.1.2 Waveguide Fabrication

Once the InGaAsP/InP wafer is grown, the waveguide structures can be defined. The overall fabrication process of our structures was based on electron beam lithography and dry etching. It can be viewed as a step process in the following manner.

First, the wafer was cleaned with acetone and blown-dried with Nitrogen gas. Following that, the wafer was coated with 400 nm of silica using plasma-enhance chemical vapor deposition (PECVD) method. A 40-nm-thick layer of chromium was deposited by electron beam (e-beam) evaporation. As the next step, we used the e-beam lithography technique, where a focused beam of electrons was used for creating patterns on the wafer covered with a 200-nm-thick layer of hydrogen silsesquioxane (HSQ) e-beam resist. Then, the waveguides were patterned using a 100-kV Jeol 9500 e-beam lithography system. The waveguide design for the experiments was based on our simulation results. The targeted waveguide width was 1.7 μm; however, in order to take into consideration fabrication tolerances, we also placed on the sample the waveguides with the widths varying from 1.1 to 2.1 μm. The patterning of the waveguide was carried out at Cornell Nanofabrication Facility (CNF). After the e-beam patterning, we developed the e-beam resist via immersing the sample in MIF 300 for 10 minutes, then rinsed the wafer and cured it at 170°C for 1 hour. This step was followed by using the e-beam-patterned HSQ mask to transfer the pattern to chromium by reactive ion etching with inductively coupled plasma (ICP-RIE). A Trion etcher was used for etching the chromium layer.

Etching InP-based materials requires dry methods that rely on ICP-RIE. This process is challenging since the chemical reaction byproducts associated with InGaAsP require high temperature to leave the surface of the material. This could not be achieved at CNF as their etcher does not have the heating option. On the other hand, in Quantum Nano Centre (QNC) at University of Waterloo, an Oxford ICP 100 system is being used that has the possibility of turning cooling system off during etching. Using this system, the chromium mask was used to transfer the waveguide pattern into silica. Finally, the silica mask was used to transfer the waveguide pattern to InGaAsP. Using

this system, the etch parameters were optimized, and the first batch of InGaAsP/InP strip-loaded waveguides was fabricated. In Figure 4.1, we summarize the fabrication process of these waveguides.

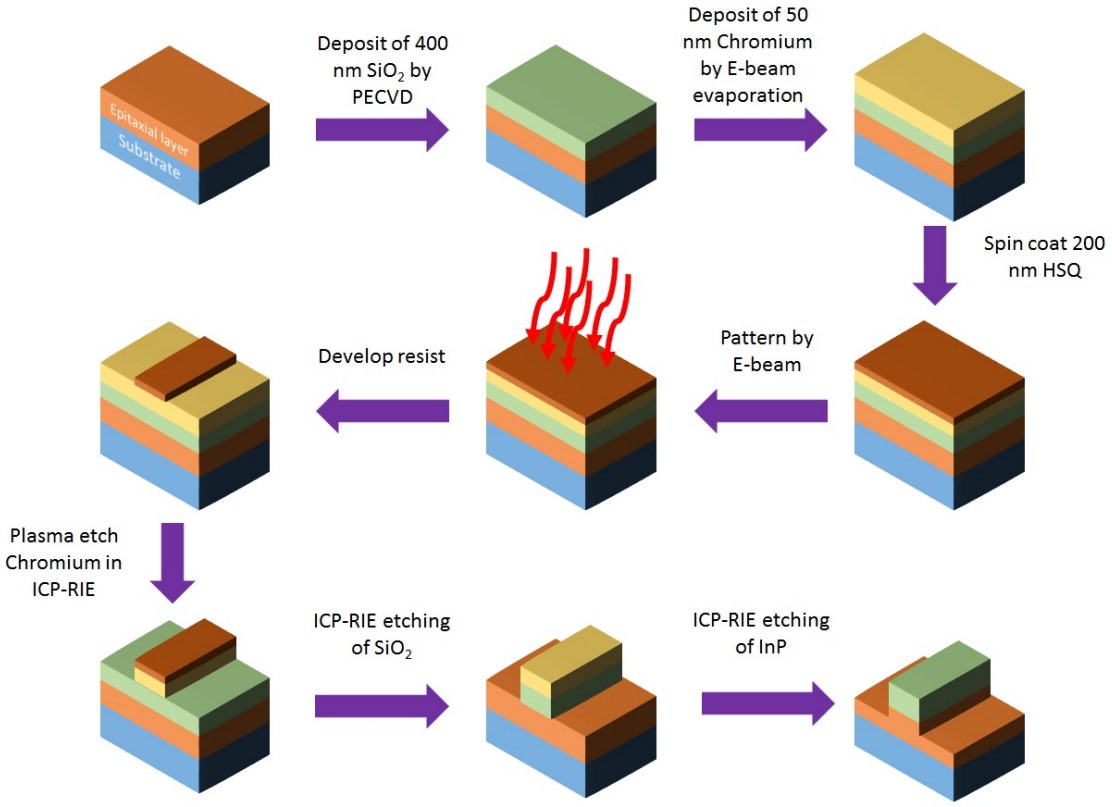

Figure 4.1: Schematic of the fabrication process used for strip-loaded InGaAsP waveguides. Silica and Chromium were deposited on top of the InP wafer, followed by the patterning of the waveguides with HSQ resist and e-beam lithography. The pattern was transferred first into the chromium mask, then the chromium was used as a mask to transfer the pattern into the silica, to prepare a hard mask for etching InGaAsP. After etching silica, InGaAsP was etched using the ICP-RIE technique.

Figure 4.2 shows the SEM (scanning electron microscope) image of the waveguide cross-section after all the fabrication steps were completed. At the inset of Figure 4.2, we show the guided fundamental TE mode profile after the light coupling into the fabricated InGaAsP/InP waveguide. The light wavelength in the experiment was $\lambda = 1.55$ μm.

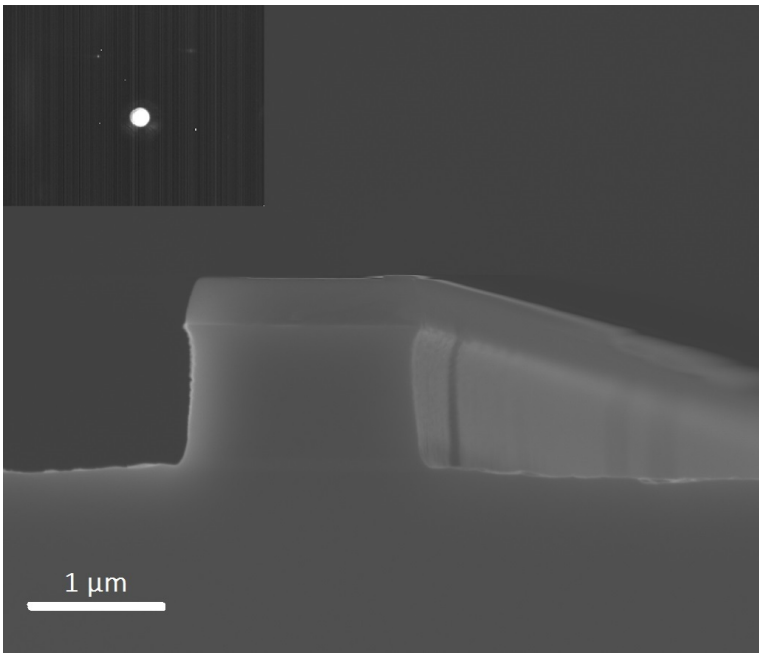

Figure 4.2: SEM image of the strip-loaded InGaAsP waveguide cross-section. The scale bar represents 1 μm. The inset shows the image of the guided mode at the wavelength $\lambda = 1550$ nm, captured by an IR camera at the waveguide output.

4.2 Loss Measurement

After the waveguides were fabricated, the sample was cleaved to get prepared for optical characterization. The first step in the assessment of the quality of the fabricated waveguides is the loss measurement. This section aims at describing this crucial step that gives an idea about the sample quality.

We have characterized the total insertion loss of the straight InGaAsP strip-loaded waveguides. The overall insertion loss is comprised of different loss contributions, such as the propagation loss, coupling loss and the reflection loss. The relation between these sources is described by the equation below:

$$L_{\text{total}} = L_{\text{coupl}} + 2L_{\text{ref}} + L_{\text{prop}}L, \tag{4.1}$$

where L_{total} is the total loss which can simply be obtained by measuring the power launched to and transmitted by the waveguide (and taking their ratio), L_{prop} is the propagation loss, and L represents

the sample length, which is 1 cm in this case. L_{prop} can be determined using the Fabry-Perot loss measurement technique. Reflection loss from interfaces, $2L_{\text{ref}}$, happens because of the refractive index difference between the semiconductor material and the surrounding medium (air). Finally the coupling loss, L_{coupl} can be estimated by subtracting the propagation and reflection losses from the total loss using Equation (4.1). The total loss and its contributions are discussed below.

The first step is to estimate the total insertion loss for our waveguide. This can be determined by comparing the power at the input and output of the waveguide. If the power at the input of the waveguide is P_{in}, and the power measured at the output of waveguide is P_{out}, then the total insertion loss is given by $10\log(P_{\text{in}}/P_{\text{out}})$. For the targeted waveguide width 1.7 μm, this value was measured to be around 18 dB.

The next step is to measure the propagation loss which can be determined by the Fabry-Perot loss measurement [67]. The loss measurement involves launching a beam into the waveguide from a tunable laser source, and taking the measurement of the output power as the function of wavelength. The schematic of setup is demonstrated in Figure 4.3. In our experiment, a *Santec* TSL-710 was used as the tunable source. The laser beam was coupled into the waveguide through a microscopic objective, and the wavelength sweep in the wavelength range around 1600 nm with the overall sweep range 1 nm and the sweep step of 1 pm has been performed to measure the output power as the function of wavelength. Figure 4.4 shows the power of the output beam as a function of wavelength for the waveguide width of 1.7 μm.

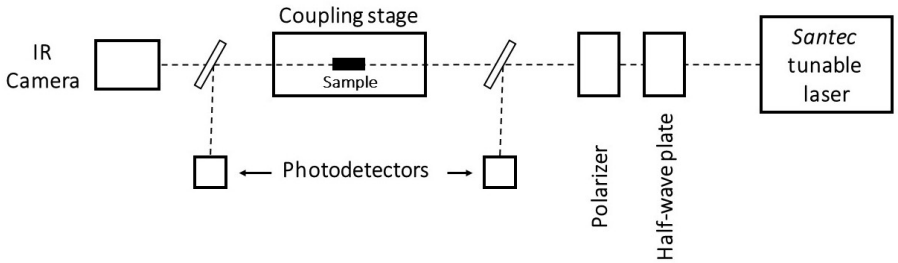

Figure 4.3: Experimental arrangement of propagation loss measurement using Fabry-Perot method.

The data analysis performed according to the following method returns the values of the propagation loss of the waveguide. The equation relating the loss coefficient α to the waveguide length L,

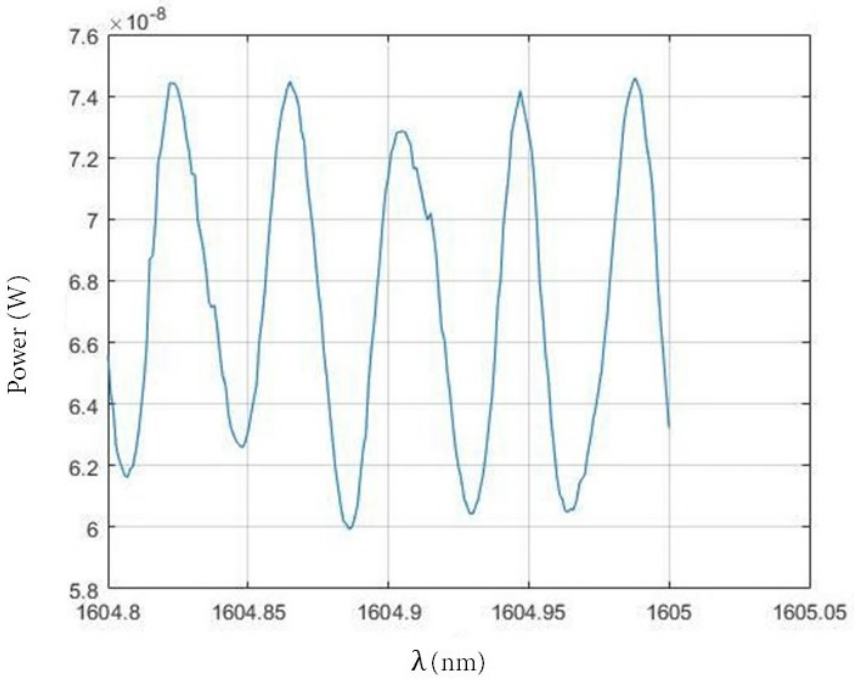

Figure 4.4: Output power as a function of wavelength for InGaAsP strip-loaded waveguide with the width of 1.7 μm.

facet reflectivity R and the ratio of minimum-to-maximum power ζ is given by Equation (4.2) [67].

$$\alpha = \frac{1}{L} \ln \frac{R(1+\sqrt{\zeta})}{1-\sqrt{\zeta}}. \tag{4.2}$$

The value of R can be obtained using Equations (4.3) and (4.4),

$$R = \left(\frac{n_{\text{eff}} - 1}{n_{\text{eff}} + 1} \right)^2, \tag{4.3}$$

$$\Delta\lambda = \frac{\lambda^2}{2 n_{\text{eff}} L}, \tag{4.4}$$

while ζ is given by the power contrast $P_{\text{min}}/P_{\text{max}}$. The values $\Delta\lambda$, P_{min}, and P_{max} can be found in Figure 4.4.

Table 4.1 shows the measured propagation loss for both TE and TM fundamental modes for different waveguide widths. We can see that the smaller waveguides have larger propagation losses; on the other hands, the larger waveguides have larger effective mode areas which results in less efficient nonlinear optical interactions.

Table 4.1: Propagation loss for the fundamental TE and TM mode in InGaAsP strip-loaded waveguides

Waveguide width (μm)	α (dB/cm) TE	α (dB/cm) TM
2.1	2.28	2.24
1.9	2.38	2.30
1.7	2.77	2.43
1.5	3.53	3.54
1.3	4.07	4.20
1.1	4.52	4.59

Following the propagation loss measurement, we estimate the reflection loss which happens at the interface between the air and material. At this interface, a fraction of the beam is reflected back to the source. This phenomenon is known as "Fresnel loss". In our the case, where the laser beam is coupled into the waveguide with no incident angel, Fresnel reflection can be estimated by

$$R = \left(\frac{n_2 - n_1}{n_2 + n_1}\right)^2, \tag{4.5}$$

where n_1 and n_2 denote the refractive indices of air and the material, respectively. The reflectivity at the interfaces between InGaAsP and air is estimated to be 30%.

Finally, the coupling loss can be estimated by subtracting the propagation and reflection losses from the overall insertion loss. The coupling loss is due to a mode size and shape mismatch when the light gets coupled in and out of the waveguide by an objective. For the waveguide width of 1.7 μm, the overall insertion loss is around 18 dB, which is the sum of the propagation loss 2.7 dB/cm, the reflection loss of $\sim$ 5.3 dB, and the coupling loss. Using Equation (4.1), the coupling loss is estimated to be $\sim$ 10 dB.

In the following chapter, we discuss the experiment on the assessment of the nonlinear optical performance of InGaAsP/InP strip-loaded waveguides.

Chapter 5

Nonlinear Optical Performance

In this chapter, we describe the results of our experimental studies on the third-order nonlinear optical interactions in InGaAsP/InP strip-loaded waveguides. In these experiments, we used the waveguide structure and the material composition that were discussed in previous chapters. In this chapter, we describe our results of nonlinear absorption measurement at the wavelength 1570 nm. In this study, we have demonstrated self-phase modulation with a nonlinear phase shift up to 2.5π, and four-wave mixing with a signal-to-idler conversion efficiency of around 50 dB. The details of these experiments are provided below.

InGaAsP is generally not suitable for passive devices in the telecom wavelength range due to relatively small energy gap values. However, we have performed our experiments at the telecom wavelengths because of the availability of the equipment and measurement tools for this range of wavelengths.

5.1 Nonlinear Optical Interactions in InGaAsP Strip-Loaded Waveguides

There is much interest and investment in studying nonlinearities of semiconductor optical waveguides because of their potentials in all-optical signal processing. Optical waveguides which have high refractive index contrast between the core and their claddings have relatively small mode areas leading to better light confinement. In addition, the smaller mode areas amplify optical field intensity

in the waveguide and, consecutively, the strength of nonlinear optical interactions.

Apart from the optical intensity and the strength of the material nonlinearity, there are other factors influencing nonlinear optical interactions in a waveguide. One of the dominant factors, strongly limiting optical switching and waveguide performance for quantum optics applications, is two-photon absorption (TPA). As discussed in previous chapters, it is desirable to set the bandgap wavelength of the material less than half of the operational wavelength. This way, bandgap energy is more than twice the photon energy, and the parasitic effects of TPA can be eliminated. However, some materials such as InGaAsP cannot wipe the influence of TPA out at the telecom C-band. This is because they have their bandgap energy (< 1.34 eV in the case of InGaAsP) near the operational photon energy at 1550 nm (0.8 eV). TPA of silicon waveguides at $\lambda = 1.5$ μm was found to be 0.45 cm/GW [68]. The influence of TPA on the nonlinear optical performance of AlGaAs/GaAs waveguides has been at the telecom wavelength has been discussed [7,19,56]. TPA of InGaAsP multi-quantum-well waveguides has been reported to have a value of 60 ± 10 cm/Gw at 1.55 μm [69], which is much larger compared to those of AlGaAs and silicon.

Another important nonlinear optical effect that occurs in a waveguide is self-phase modulation (SPM). This effect involves spectral changes (breoadening) and nonlinear phase shift acquired by the optical beams propagating through a waveguide. A nonlinear phase shift of π has been reported for silicon waveguides at 60 W input peak power [68]. This value increases to $\sim 2.5\pi$ for InGaAsP multi-quantum-well waveguides at the input peak power of 3.8 W [69].

In this section, we briefly summarize the structure and properties of the InGaAsP waveguide that was used for the nonlinear optical experiments in this thesis work. Following that, we will discuss the experimental setup and characterize the nonlinearity of InGaAsP/InP optical waveguide in terms of TPA and SPM at the telecom wavelength. To the best of our knowledge, there has been no experimental work on measurement of TPA coefficient for nonlinear passive InGaAsP/InP waveguides.

5.1.1 Waveguide Structure and Properties

The design and choice of the material composition for InGaAsP/InP waveguides was discussed in detail in Section 3.2. The structure of the waveguide used in our experiments is shown in Figure 5.1. This waveguide has relatively large dimensions and is known as strip-loaded waveguide. We are interested in such waveguides mainly because of their low propagation loss. The thickness of the

guiding layer is set to 0.4 μm in order to minimize the effective mode area. The effective mode area calculated using the commercial software *Lumerical Mode Solutions* was around 1.7 μ m^2 at the telecom wavelength 1550 nm. The composition of the guiding layer was $In_{0.63}Ga_{0.37}As_{0.8}P_{0.2}$ with the refractive index of 3.58 at 1550 nm [70]. The refractive index of InP claddings is 3.17 [71] which gives the index contrast of 0.41 between the core and claddings at 1550 nm. Such waveguide is capable of guiding light from the telecom wavelengths to around 3 μ [72]. The wafer was grown through molecular beam epitaxy (MBE) and then patterned via electron beam lithography. We etched the sample using a reactive ion etching with inductively coupled plasma (ICP-RIE). We

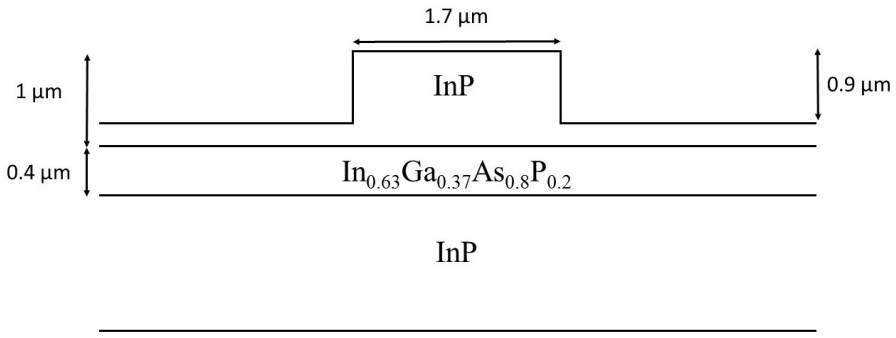

Figure 5.1: Structure and dimensions of InGaAsP/InP strip-loaded waveguide.

describe below our nonlinear optical experiments performed with the waveguide structure described herein.

5.1.2 Two-Photon Absorption

Figure 5.2 shows the experimental setup that we used for measuring the two-photon absorption coefficient and for SPM experiments. As the light source, a mode-locked Ti:Sapphire laser with a repetition rate of 76 MHz has been used to pump the optical parametric oscillator (OPO). The wavelength of the Ti:Sapphire laser was set to 830 nm, and the output of the OPO was tuned to 1570 nm. The pulse durations of the laser was around 3 ps. A linear polarizer was used in order to set the input polarization either to TE or to TM, while a half-wave plate in combination with the linear polarizer allowed to change the input optical power in our experiment. The laser beam was butt-coupled to the waveguide with the use of an objective lens with magnifying power 40×. The guided mode was captured and observed with the help of an infra-red camera. To measure the TPA coefficient β_2 of the sample, we use the nonlinear transmission (NLT) method, also known

as nonlinear absorption experiment [73]. NLT, along with z-scan experiment, is one of the most efficient ways to measure TPA coefficient. In this method, the transmitted output power is carefully measured as the input power at the entrance to the waveguide varies. The incident and transmitted powers are measured with a pair of photodetectors.

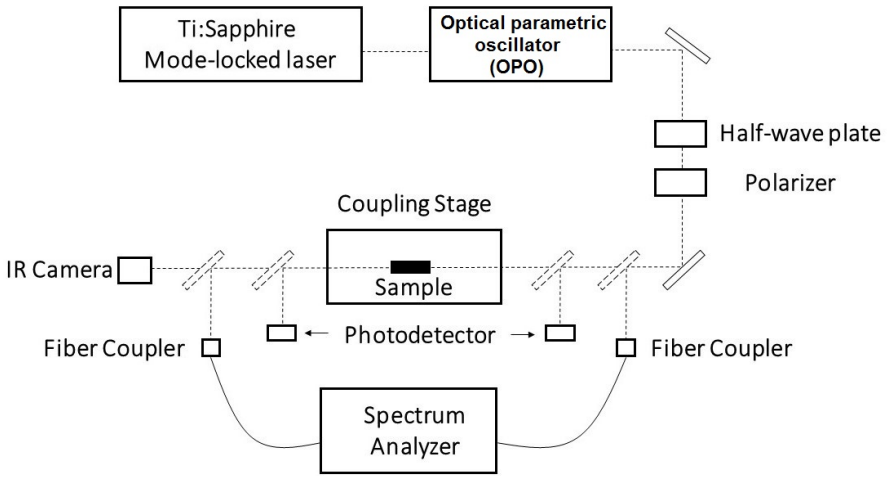

Figure 5.2: Experimental setup for the measurement of two-photon absortion and self-phase modulation of InGaAsP/InP strip-loaded waveguide.

Figure 5.3 represents the transmitted power as a function of the average launched power into the waveguide for both TE and TM polarizations. The points represent the measured values on the output power, and the solid and dashed lines represent the least-square fit to the experimental data for TM and TE polarizations, respectively. The experimental curves exhibit strong saturation behavior which is an indication of the nonlinear absorption. At high input powers, the optical limiting behavior is obvious, which is caused by TPA and free-carrier absorption. TPA is the result of proximity of the band-edge (1.45 μm) to the operational wavelength (1.58 μm). The free carriers generated via TPA can absorb certain amount of photons by linear absorption. These free carriers also limit the nonlinear optical performance of the waveguide at the experimental wavelength range.

The measurement results showin in Figure 5.3 were used to extract the value of the TPA coefficient β_2. We start with the equation relating the optical intensity of the incident beam I with the distance the beam has traveled through the waveguide z [74]:

$$-\frac{dI}{dz} = \alpha I + \beta_2 I^2. \tag{5.1}$$

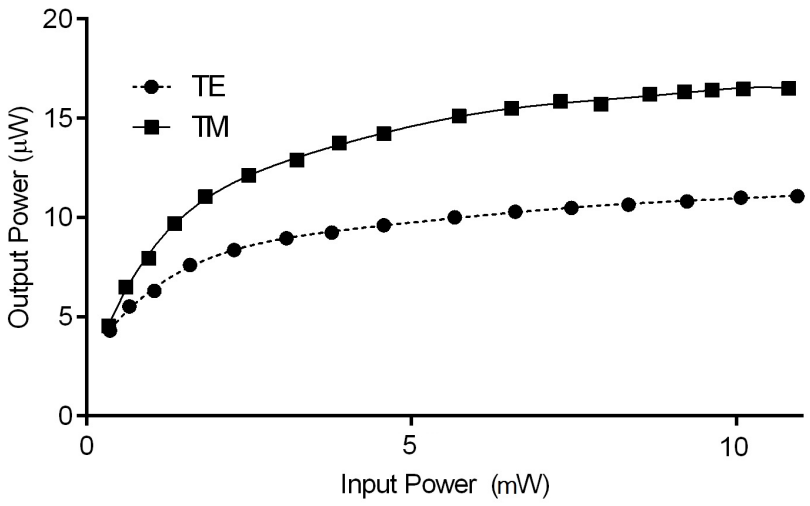

Figure 5.3: Output vs. input power for the TE and TM fundamental modes.

Here α represents the linear absorption coefficient. This equation can be satisfied by [69]

$$\frac{1}{T} = e^{(\alpha L)} \frac{L_{\text{eff}}}{A_{\text{eff}}} \beta_2 P_{in} + e^{(\alpha L)}, \tag{5.2}$$

in which T refers to the power transmission ratio ($P_{\text{out}}/P_{\text{in}}$), $L_{\text{eff}} = (1-exp(-\alpha L))/\alpha$ is the effective path length, L represents length of the sample, and A_{eff} is the effective mode area.

The TPA coefficient can be obtained by carefully measuring the transmission for different input powers and fitting Eq. 5.2 to these results. Figure 7 shows the reciprocal transmission as a function of the input peak power. The experimental data are indicated with the black points. The gradient of the line fitted to experimental data points is proportional to β_2. Therefore, the TPA coefficient β_2 can be obtained by the best line fit to the experimental data, as shown in Figure 5.4 with the solid lines. The intercept of the line with the vertical axis demonstrates the linear loss of the waveguide. The calculated TPA coefficient has the value of $\sim$ 15 cm/GW. For comparison, our value of β_2 is almost one quarter of the value reported for InGaAsP/InP multi-quantum-well waveguides [69].

5.1.3 Self-Phase Modulation

As discussed earlier, SPM is the change in the phase of the launched optical pulse into the medium, due to the nonlinearity of the material medium. As a result, the spectrum of the pulse after its propagation through a nonlinear optical medium will be generally broader than the spectrum of the

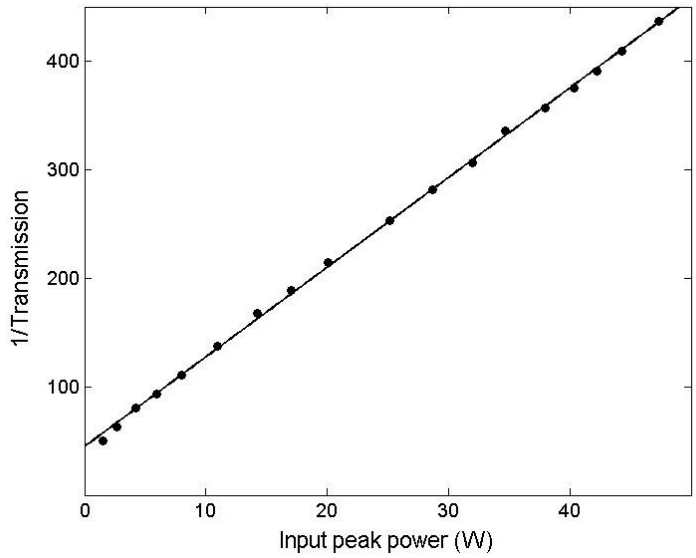

Figure 5.4: Reciprocal transmission vs. incident peak power.

launched pulse. For our experiments with SPM we use the same setup as we displayed for TPA measurement (see Figure 5.2). The intensity of the input pulse can be controlled via an optical attenuator to compare the spectra of the transmitted pulses at different intensities. As we discussed in Section 5.2.2, an optical limiting behavior was observed at high input intensities, which is mostly caused by TPA. The free carriesrs generated via TPA can influence the nonlinear performance of the device. In the absence of free carriers, spectral broadening of the pulse is expected to be symmetrical as the input power increases, however, this in not the case here.

Figure 5.5 represents the spectra measured at the output of the InGaAsP/InP strip-loaded waveguide, recorded for different values of the input peak power. The spectrum at the bottom represents the lowest-power output spectrum, and the uppermost spectrum shows the spectrum corresponding to the highest power launched into the waveguide. As the incident optical power increases, moving from the lower to the upper trace, the spectral broadening becomes evident. This broadening is a manifestation of the self-phase modulation experienced by the optical beam propagating through the InGaAsP/InP waveguide. The values of the nonlinear phase shift acquired by the optical beam after propagating through the waveguide, estimated from the recorded spectra [48], are shown in the legend of Figure 5.5. Despite the fact that the nonlinear absorption was strong, the nonlinear phase shift up to $\sim 2.5\pi$ at the input peak power of around 40 W has been observed. For comparison, a nonlinear phase shift up to 6π was observed in AlGaAs strip-loaded waveguides [7].

The nonlinear phase shift in chalcogenide glass waveguides was found to be 1.5π [14].

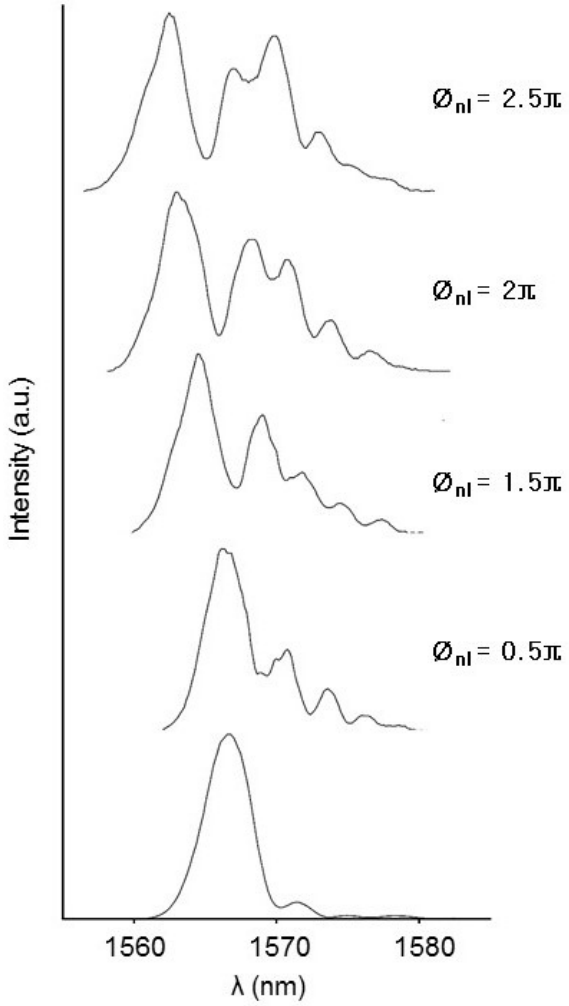

Figure 5.5: Self-phase-modulation experimental data. The launched pulse intensity increases from bottom to top. The nonlinear phase shift of up to 2.5π has been observed at the input peak power of 40 W.

Using the results of the spectral measurements, presented in Figure 5.5, we can now estimate the value of the Kerr coefficient n_2 for our waveguide. The intensity-dependent nonlinear phase shift ϕ_{NL} due to SPM is given by [26]

$$\phi_{\mathrm{NL}} = n_2 k_0 L I, \tag{5.3}$$

in which $k_0 = 2\pi/\lambda$, L is the sample length, and I is the incident beam intensity. This equation was used in order to estimate the value of the Kerr coefficient of InGaAsP/InP strip-loaded waveguides in our experiment. The calculated value of the Kerr coefficient was on the order of 10^{-13} cm^2/W.

On the other hand, the n_2 value of $Al_{0.18}Ga_{0.82}As$, which is the benchmark material for nonlinear integrated optical devices based on III-V semiconductors, is around 1.5×10^{-13} cm^2/W [19]. The Kerr coefficient of silicon was reported to be 4.2×10^{-14} cm^2/W at telecom wavelength [25]. Our value of n_2 is similar to the one measured for AlGaAs. Thus, one can expect that the nonlinear optical performance of our waveguides could be comparable to that of AlGaAs waveguides, albeit a different spectral range (outside the TPA zone) is explored.

We now have sufficient information in order to characterize the nonlinear optical performance of the InGaAsP/InP strip-loaded waveguides in terms of the figure of merit F, expressed as [75]

$$F = \frac{n_2}{\lambda_0 \alpha_2}, \tag{5.4}$$

and the nonlinear coefficient γ, defined as

$$\gamma = \frac{2\pi\, n_2}{\lambda_0\, A_{\text{eff}}}. \tag{5.5}$$

The figure of merit characterizes the potentials of the material itself for the nonlinear optics at the specific wavelength λ_0, while the nonlinear coefficient describes the performance of the nonlinear optical waveguide characterized by its effective mode area A_{eff} at the wavelength λ_0. The nonlinear optical performance of a waveguide is best when both the parameters are maximized, which can be achieved by a proper selection of the material (for the figure of merit), and by a proper design of the waveguide (for the nonlinear coefficient). For a nonlinear material to be considered efficient, the condition $F > 1$ must be satisfied. Based on the measured and estimated values of n_2 and α_2 in our experimental study, InGaAsP has $F \approx 0.043$, which is consistent with the fact that the operation wavelengths 1530–1570 nm fall within the range of strong two-photon absorption. The nonlinear coefficient $\gamma \approx 36.85$ m^{-1}W^{-1}, characterizing the performance of the InGaAsP/InP waveguides as nonlinear devices, is almost three times larger than that of similar devices based on AlGaAs [7]. This can be attributed to the fact that we have designed our InGaAsP/InP waveguides in a way that their effective mode area is minimized to the level of under 2 μm^2, compared to the values over 4 μm^2 reported in [7]. It is thus possible to exploite the full potential of such waveguides by a proper selection of the operation wavelength which, in our case, should be close to 2 μm.

5.1.4 Four-Wave Mixing

Four-wave mixing experiments is the central part of the demonstrations of the nonlinear optical performance of InGaAsP/InP strip-loadede waveguides. This effect can be useful in many all-optical signal processing operations such as wavelength conversion, optical time-division (de)multiplexing, *etc* [76, 77]. We have successfully realized such an experiment.

An efficient FWM is more likely to be achieved in the absence of nonlinear absorption. Although this is not the case for our waveguides at the telecom wavelength range, one can expect that the small effective mode area of our waveguide can compensate for the adverse effect of TPA on the efficiency of the FWM.

Prior to recording FWM data collected from our waveguides, we first maximized the four-wave mixing signal by setting the right experimental conditions. We used the same setup as that built for SPM and TPA measurements, with the only difference of adding the second optical beam, consisting of a tunable CW laser amplified by an erbium-doped fiber amplifier (EDFA). The resulting setup is demonstrated in Figure 5.6. The beams from the OPO (pump) and the EDFA (signal) are coupled into the waveguide by being mixed at a non-polarized 50-% beam combiner cube. The polarization states of the two beams were controlled independently via two sets of polarizers in combination with half-wave plates, inserted in each beam.

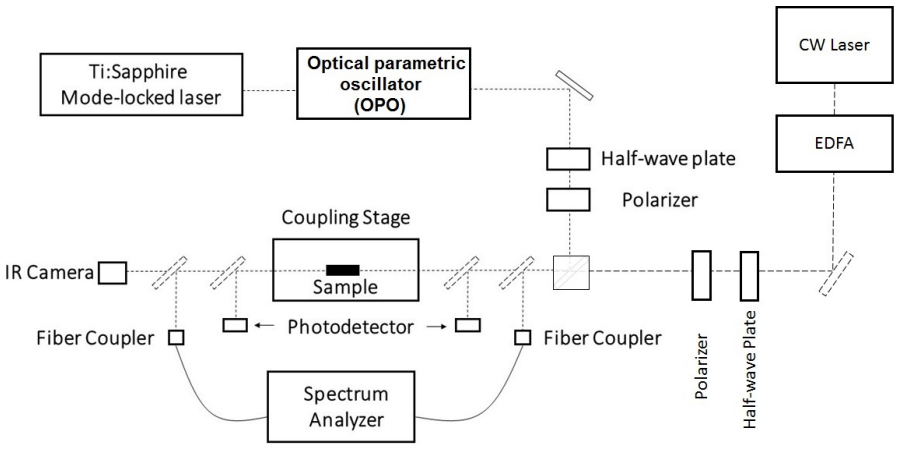

Figure 5.6: Experimental setup for FWM measurements.

In Figure 5.7, we show the outcome of the measurements, obtained for a 1.7-μm-wide $\sim$ 5-mm-long strip-loaded waveguide with the pump wavelength centered at 1568 nm and the cw signal tuned between 1544 and 1569 nm. In this figure, we show the combined output spectra of the pump and

cw signal at the output of the waveguide. These spectra indicate the presence of an extra spectral component, the generated idler peak, resulting from the four-wave mixing interactions (highlighted with the red shaded area). According to the simulations discussed in Chapter 3, TE-polarized beam demonstrates a smaller dispersion at the telecom wavelengths compared to that of the TM polarization. On the other hand, the effective mode area for the TM-polarized light is smaller; thus, the FWM efficiencies for both the polarizations are more or less the same. Here, we present the FWM for TM polarized beam in Figure 5.7.

The characteristics that we have observed in our experiment are comparable to those demonstrated with AlGaAs waveguides of similar geometry [7]. The overall conversion range (the difference in wavelength between the maximally separated signal and idler spectral components) was $\lambda_{\mathrm{i}} - \lambda_{\mathrm{s}} = 45$ nm, limited by the material dispersion which is the dominant dispersion mechanism in strip-loaded waveguides (see the arguments provided in [7]). Indeed, the material dispersion of InGaAsP in the vicinity of 1568 nm is $D_{\mathrm{mat}} = -19500$ ps/nm/km, while the simulated overall dispersion with the waveguide contribution taken into account is around $D_{\mathrm{tot}} = -17200$ ps/nm/km. The latter value is only slightly offset with respect to the very high value of the material dispersion and lends to the characteristic dispersion length, defined as

$$L_{\mathrm{D}} = \frac{T_0}{D_{\mathrm{tot}}\,\Delta\lambda_{\mathrm{max}}} \tag{5.6}$$

in terms of the pulse duration T_0 and maximum wavelength separation between the pump and signal $\Delta\lambda_{\mathrm{max}} \approx 22$ nm, comparable with the length of the waveguide. The waveguides have the length $L = 5$ mm, while $L_{\mathrm{D}} \approx 8$ mm. The lack of dispersion management in our devices thus contributes to the very low efficiency and limited tuning range of the FWM process.

We also measured the maximum tuning range for our waveguide. We define the tuning range as the difference in the wavelength between the cw signal and the generated idler. Based on the data presented in Figure 5.7, the maximum tuning range that can be achieved in our waveguide is around 45 nm, which is similar to the values reported for AlGaAs strip-loaded waveguides in [7]. The other important factor to be considered is the achievable FWM conversion efficiency. By the conversion efficiency, we mean the ratio of the generated idler power to the output cw signal power. The maximum conversion efficiency of ~ -50 dB was achieved. The value of -38 dB was reported for AlGaAs nanowires [16] in the wavelength range where two-photon absorption was negligible. We need to emphasize that, in general, nanowires exhibit more efficient optical nonlinearity compared

to strip-loaded waveguides due to the possibility of dispersion engineering and even more compact mode size in them. However, the values we have achieve for our InGaAsP strip-loaded waveguide are comparable to those reported for well-studied AlGaAs strip-loaded waveguides. In our experiment, the limiting factor was the strong TPA in the telecommunication wavelength range.

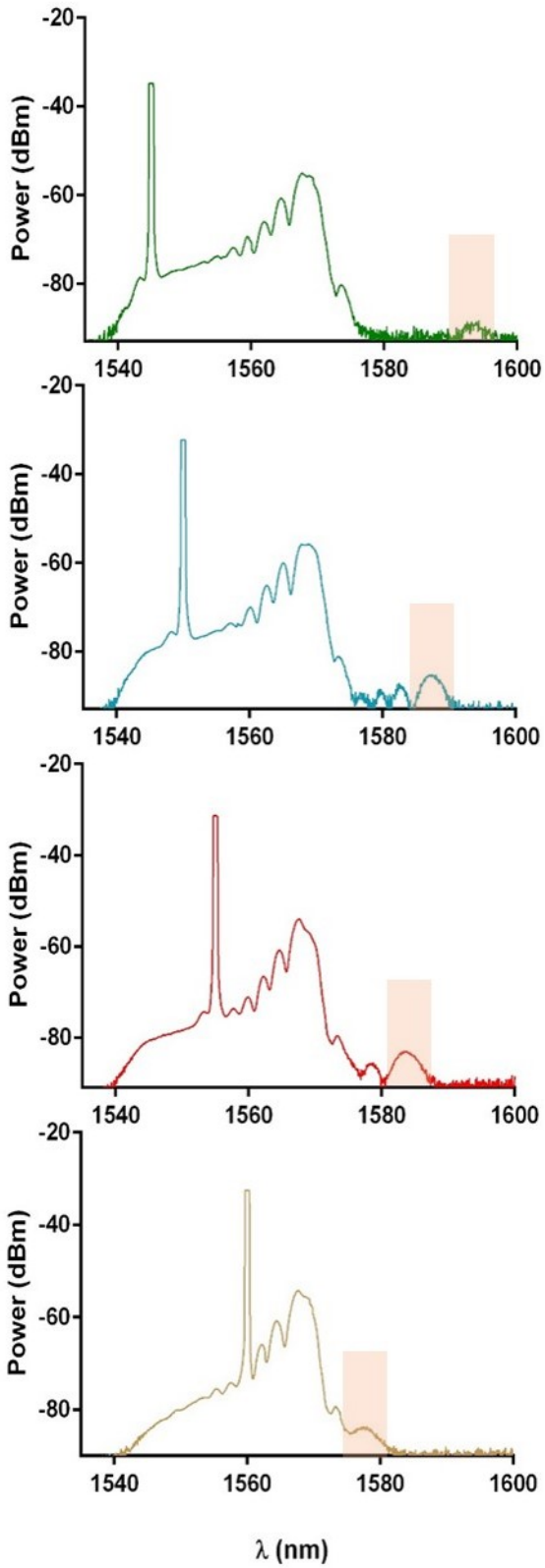

Figure 5.7: Four-wave mixing experimental data. The pump wavelength was fixed at 1568 nm, and the signal wavelength was tuned in the range between 1544 and 1559 nm. The corresponding generated idlers are highlighted with shaded area.

Chapter 6

Study of a Spot-Size Converter for the Taper-Assisted Vertical Integration Platform in InP

So far in this thesis, we have been focusing on identifying promising III-V semiconductors for nonlinear photonics, and on assessing specific materials for applications in photonic integrated circuits and optical communication networks. In this chapter, we will discuss a realistic commercial material platform which finds many applications in integrated optics (primarely in optical communications).

Through the term of my Master's program, I had an opportunity to gain experience that extends beyond the academia research. I had a chance to collaborate with *Intengent* III-V Photonics Company under the supervision of Dr. Valery Tolstikhin. We conducted a research on one of the most generic building-blocks of Taper-Assisted Vertical Integration (TAVI) photonic integrated circuits for transmitters and receivers in optical fiber communication systems: a spot-size converter based on InP technology. TAVI, in general, is defined by building lateral tapers in a specially designed multilayer epitaxial structure. In the case of spot-size converter, this structure permits an adiabatic transition of guided light from the semiconductor waveguide to the optical fiber, or vice versa. In this study, we describe our work on the optimization and tolerance analysis of such structure.

Light coupling between an indium phosphide (InP)-based photonic integrated circuit (PIC) and a standard single-mode fiber (SSMF) is a well known problem that requires attention. The

primary reason to that is a mode size and shape mismatch between a PIC waveguide (PWG) and a standard single-mode fiber (SSMF) optical modes. The former is usually much smaller and has either rectangular or elliptical shape, whereas the latter is relatively large and circular in shape. For this reason, direct coupling between the two requires focusing with a precise alignment, while the overall coupling efficiency is still humpered by a significant coupling loss due to the mode shape mismatch, and by a low displacement tolerance. One of the best solutions to the problem is to implement a spot-size converter (SSC) that transforms the PWG mode to be closely matched with the SSMF mode at the chips facet. The particular designs and implementations of such an on-chip SSC depend on the PIC integration platform and fabrication process [78, 79]. In any case, an SSC performs a gradual expansion of the PWG mode in vertical (along the epitaxial growth axis) and lateral (in the plane of the epitaxial growth) dimensions, such that it matches the SSMF mode at the facet. One possible approach is based on the use of a diluted coupling waveguide (CWG) with the optical mode closely matching that of the SSMF, and an evanescent field coupled to it [80]. Then, by lateral down-tapering the PWG, an adiabatic transition of the guided light from the PWG into the CWG (or vise versa) can be achieved, thereby reducing the problem to that of the CWG-to-SSMF coupling. The performance of an SSC in terms of the coupling loss and the displacement tolerance depends largely on the design of the PWG, the CWG, and the taper. It has been shown that using a multi-step lateral tapering between the PWG and the CWG provides an efficient solution to the coupling problem, and is fully compatible with the taper-assisted vertical integration (TAVI) platform a regrowth-free photonic integration technology, in which functional waveguides are vertically integrated within a common epitaxial structure, while adiabatic vertical transitions between them are achieved by means of their lateral tapering [81].

Even though the concept of the multiple-step lateral tapering SSC and its natural suitability for a vertical integration with other PIC elements are well established, there has been no report on exploration the limits, nor optimization, nor tolerance analysis of such a design. In this chapter, we address these issues by using statical Monte-Carlo simulations.

6.1 SSC Base Structure

In the TAVI-based PICs, the functional waveguide devices, active (such as lasers or photodetectors) and passive (such as beam or wavelength splitters/combiners), are coupled to passive waveguides for on-chip optical interconnecting and routing. Therefore, PICs input/output optical ports should

also be connected to the passive waveguides. If properly designed and processed, such waveguides both feature low propagation loss and are suitable for taper-assisted coupling to the diluted CWG.

A generic frame of SSC consists of a multilayer structure. It is epitaxially grown on a semi-insulating (SI) or an unintentionally doped InP substrate in one epitaxial growth step and consists of only two semiconductor materials: InP and quaternary InGaAsP, lattice-matched to InP. These materials have different bandgaps and hence different refractive indices; the refractive index of InP is lower compared to that of InGaAsP. Single-mode vertical guiding in PWG is achieved by sandwiching a relatively thick InGaAsP layer between two InP layers. To achieve the same in a diluted CWG having much bigger mode size, much thinner InGaAsP layers can be interleaved with thicker InP layers, together acting as a diluted CWG core. This layer structure allows for a four-step lateral taper. The resulting waveguide structure is schematically depicted in Figure 6.1, where the light-blue colored layers indicate the quaternary InGaAsP and the dark-blue colored layers indicate InP. The top-to-bottom structure consists of: (i) PWG the shallow-etched (etch does not penetrate the quaternary waveguide core) ridge waveguide; (ii) *Transition Waveguide 1 (TWG1)* the deep-etched (the etch goes through the quaternary waveguide core) ridge waveguide; (iii) *Transition Waveguide 2 (TWG2)* the shallow-etched (the etch does not penetrate the GaInAsP-InP diluted waveguide core) ridge waveguide (special case of the more general rectangular waveguide, where the etched core layer is located above the cladding); (iv) *Coupling Waveguide (CWG)* the deep-etched (the etch goes through the GaInAsP-InP diluted waveguide core). In reality, all four lateral guides may not be present simultaneously in any device cross-section, but their relative position in the layer stack still follows the schematics of this sketch. Such an SSC is a rather complex device with a performance defined by an interplay of its many design parameters that outline vertical and lateral guiding in the four-step lateral taper SSC. While the design optimization target low SSMF-to-PWG coupling loss and high SSMF displacement tolerance is clear, it is hard to expect that it could be met by lining up that many design parameters intuitively. On the other hand, the design of experiment would be a cumbersome and expensive task to undertake, since there are not just many layout variances (which could be combined on the same epitaxial wafer), but also many epitaxy designs (which require different epitaxial wafers) should be explored. Hence, an adequate numerical method of optimization of the base SSC design is needed.

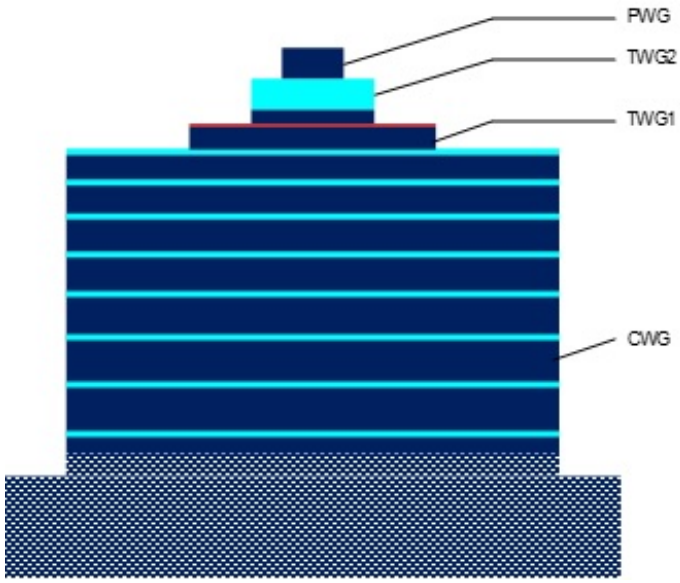

Figure 6.1: Schematic cross-section of the PWGCWG twin-guide SSC featuring four-step lateral taper. In reality, all four lateral guides may not be present simultaneously in any device cross-section, but their relative position in the layer stack still follows the schematics of this sketch.

6.2 Design Optimization

As discussed in the previous section, the TAVI SSC is an intricate device and its performance relies on many design parameters, *e.g.*, epitaxial layer refractive indices and layout dimensions. Each random combination of these parameters can significantly alter the performance of the device. Therefore, achieving the optimized design, meaning the minimal loss at best alignment, can be tricky and is not only based on intuition. However, the optimization problem can be approached based on Monte-Carlo simulation, which is commonly used to model the probabilities of different outcomes of a process. Similar methods based on randomly generating initial population of individuals, such as genetic and evolutionary algorithms, have been implemented for optimization of on-chip photonic devices [82, 83]. In this study, we evaluate the coupling loss, defined as the mode overlap of SSC and SSMF at the facet of the device, as the SSC performance feature. The thickness of the epitaxial layers and the widths of the transition waveguides have the most contribution to the coupling loss, and are considered as the key design parameters in our study. The Monte-Carlo simulation is done by assigning each key design parameter a uniformly distributed value over a specific range of variance. Subsequently, random sets of design parameters can be generated, and the coupling efficiency can be calculated for each of them. By running over 1000 simulations, we narrow down the range of

design parameters to those yielding the least coupling loss, which is 0.35 dB. The coupling losses were calculated by an overlap integral between the fiber mode and the field at the input of SSC. The layered structure of the optimized SSC cross-section at the facet is shown in Table 6.1. In this structure, there are total number of 23 layers (excluding the substrate). The CWG core layer is a combination of interleaving InP and GaInAsP layers. With the N GaInAsP layers having the same thickness while the thickness of N-1 InP layers between them can vary.

Table 6.1: Layer structure of the optimized four-step lateral taper SSC

Layer #	Description	t (μm)	n_{1310}
1	InP PWG-AWG Separation	0.527	3.2026
2	GaInAsP PWG Core	0.405	3.2565
3	InP CWG-PWG Separation 1	0.254	3.2026
4	GaInAsP Etch Stop	0.005	3.2140
5	InP CWG-PWG Separation 2	0.232	3.2026
6	GaInAsP CWG Core 1	0.032	3.2565
7	InP inter-CWG Separation1	0.361	3.2026
8	GaInAsP CWG Core 2	0.032	3.2565
9	InP inter-CWG Separation 2	0.456	3.2026
-	———————		
2N+2	GaInAsP CWG Core N-1	0.032	3.2565
2N+3	InP inter-CWG Separation N-1	0.361+0.095(N-2)	3.2026
2N+4	GaInAsP CWG Core N	0.032	3.2565
2N+5	InP Buffer	0.3	3.2026

The layout, as shown in Figure 6.2, is crafted in a way that the end-to-end insertion loss remains low through the propagation of the launched beam. The field simulations were performed with a three dimensional (3D) finite difference beam propagation method using RSoft computer-assisted design (CAD) beam propagation method (BPM). The evolution of the beam thorough the structure is demonstrated in Figure 6.3 (a). The total length of SSC, meaning the distance between the straight sections of CWG and PWG, is considered to be 1400 μm. The assumption for the SSC length is reasonable, because it is neither too short to have an incomplete mode conversion, nor too long to significantly increase the radiation loss. A power conversion efficiency of 95% was obtained through the simulation.

The gradual change of the effective index as a function of the propagation distance, as shown in

Figure 6.3 (b), indicates the smooth adiabatic transition of the guided mode from SSMF to the device WG with the small-size optical mode. The flat-index regions at both ends of the plot correspond to the straight sections of CWG and PWG.

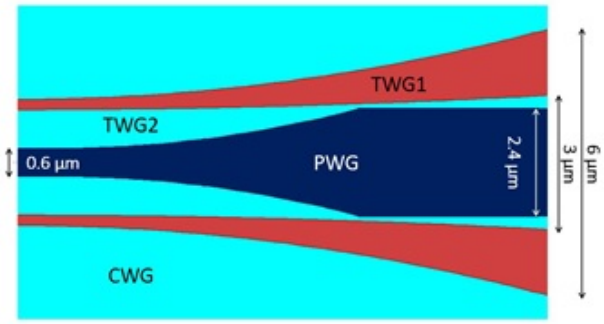

Figure 6.2: Schematic top layout of the four-step lateral taper SSC featuring the PWG, TWG1, TWG2, and CWG with the cross-sections outlined in Figure 6.1.

6.3 Tolerance Analysis

We also studied the tolerance of the optimized cross-section and layout. We used the commercial software PhoeniX OptoDesigner to perform this simulation. Figure 6.4 shows the contour map of the coupling loss as a function of fiber displacement with respect to the optimal alignment. In this analysis, the fiber is moved horizontally and vertically at the facet of the SSC. One can see from the plot that the fiber displacement sensitivity for the coupling loss of 1 dB (*i.e.*, ∼79% coupling efficiency) is limited horizontally to a displacement of around 6.5 μm in both directions. However, an asymmetric behavior with respect to a vertical displacement can be seen, which is due to the lack of vertical symmetry in the structure. The 1 dB coupling loss penalty is limited to around 8-μm displacement in downward direction, and to around 7 μm in upward direction. It can be seen that the SSC has higher tolerance laterally. The reason is that the SSC mode is compressed vertically between the air above and the InP substrate below. On the other hand, the structure is assumed to be infinite in the lateral dimension. The total end-to-end loss of the SSC as a function of the horizontal and vertical displacement of the fiber with respect to its optimal position is represented in Figure 6.5. It can be seen from the figure that the 1-dB loss displacement tolerance is around 10 μm and 7 μm in the horizontal and vertical directions, respectively. At the optimum position

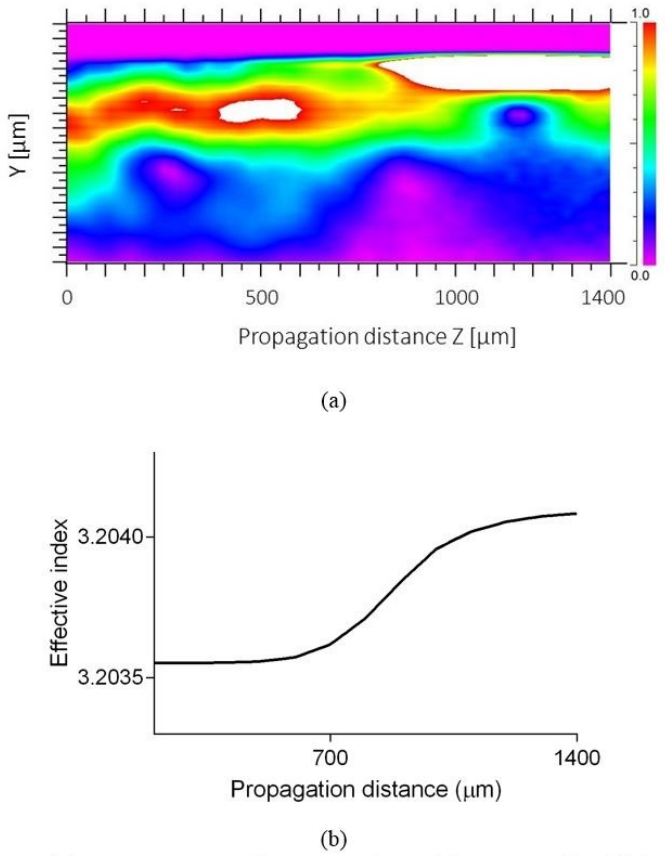

Figure 6.3: (a) SSC structure with contour plots of the propagating filed. (b) Effective index change through the structure.

the total loss is around 0.5 dB. The shape of the tolerance profile remains approximately the same when the polarization of the input beam changes.

We have also studied the tolerance of the optimized SSC design to manufacturing errors. The tolerance can be defined mainly by two factors: the epitaxial structure variance, in particular, the material composition and the thickness of layers, and the wafer fabrication variance, notably, the PWG ridge width. Therefore, we studied conservative fabrication tolerances of different parameters, including the material composition of the quaternary layers represented by the range of their refractive indices, the thickness of all quaternary and most of the InP layers, and the width of PWG ridge at the taper tip. Each of these factors are considered as a random parameter over a certain tolerance range. For all the parameters, a Gaussian distribution with a standard deviation equal to one half of the tolerance range, is assumed.

To conduct the tolerance analysis in the presence of the manufacturing errors, we performed a Monte-Carlo process of randomly varying the variable parameters, calculating the performance in

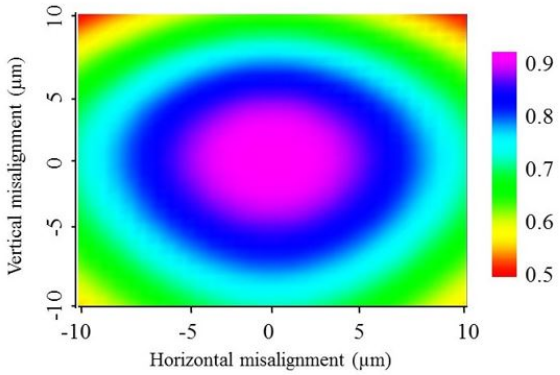

Figure 6.4: Coupling efficiency as a function of the horizontal and vertical misalignment. The mode overlap between the fiber and SSC at the best alignment is around 92%.

terms of coupling loss for each combination of the parameters, and estimating the probability of the outcome events. Figure 6.6 shows the histogram of the results along with their estimated cumulative distribution function (CDF). From this figure, it can be interpreted that the best alignment yields the coupling loss of around 0.2 dB. In addition, one can see from CDF that almost 90% of the events will have coupling loss less than 1 dB.

6.4 Conclusions

In conclusion, a multiple-step lateral taper SSC design compatible with the regrowth-free TAVI platform based on InP is proposed, optimized, and evaluated with regards to its key performance features and stability against manufacturing tolerances. By using the Monte Carlo method for multiple parameter optimization and tolerance analysis, it is shown that the four-step lateral taper SSC is capable of as low as 0.35 dB coupling loss, and has as high 1-dB displacement tolerance as $\pm 7\ \mu$m, while remaining fairly stable against manufacturing imperfections.

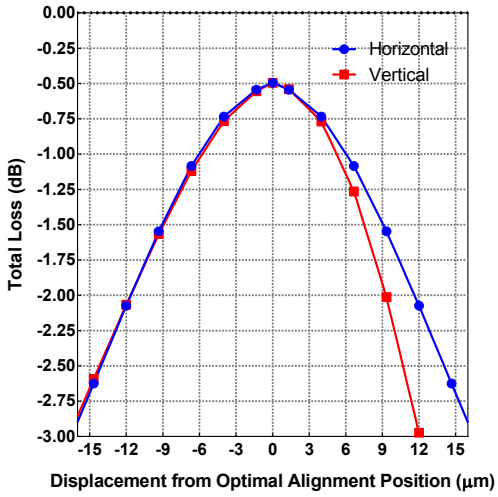

Figure 6.5: Total end-to-end loss of the designed SSC as a function of the horizontal and vertical displacement of the fiber. The total loss at the best alignment is around 0.5 dB.

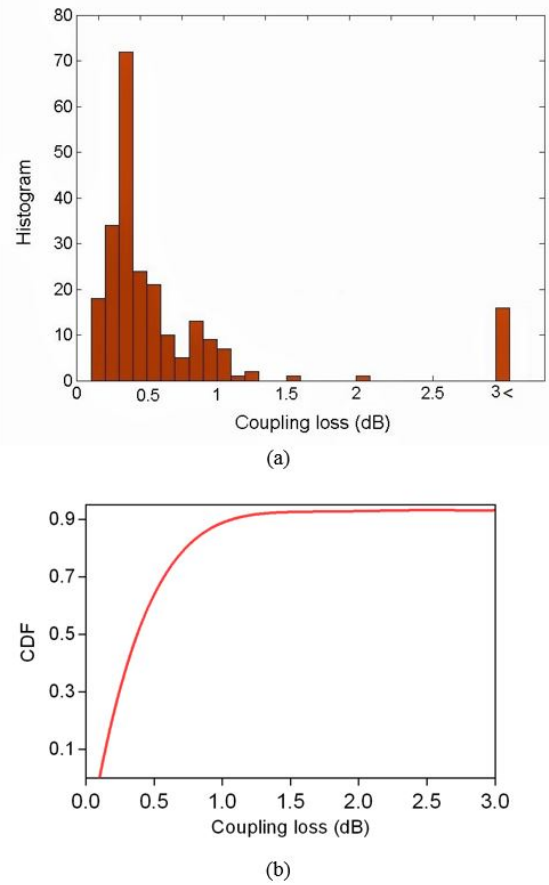

Figure 6.6: (a) Histogram and (b) CDF of tolerance analysis of the SSC coupling loss to manufacturing errors.

Chapter 7

Summary

Because of the growing consumption of internet bandwidth and the expanding demand for bandwidth-hungry applications, the conventional techniques of optical signal processing electronically can no longer be fully practical. On the other hand, the process size in electronics is already approaching the fundamental limit of a few nanometers, and the more frequent transistor switching aggravate the problem of heat dissipation. All-optical signal processing can be a solution to overcome these limitations, which can be implemented only by relying on nonlinear optical interactions. As discussed in Chapter 1, in general, it is interesting to study III-V semiconductor materials for integrated optics since they demonstrate high nonlinearity. The purpose of this thesis is to identify new promising material candidates, out of class of III-V semiconductors, for nonlinear photonic devices on-a-chip.

As the first step of this long-term study, we identified two interesting material candidates: the quaternary compounds AlGaAsSb and InGaAsP. This thesis work is limited to consideration of these two materials, and four waveguide design based on them. Although there is no sufficient data on the nonlinear optical performance of AlGaAsSb and InGaAsP, based on the available partial information, we expect the strength of the nonlinear optical interactions in these compounds to be comparable to that observed earlier in AlGaAs waveguides. AlGaAsSb waveguides have potentials of application in the telecom wavelength range, while InGaAsP nonlinear waveguides are expected to extend the operation range of the existing InGaAsP laser sources to longer wavelengths. We present several waveguide designs based on these materials. Numerical calculations and modal analysis were performed to determine the waveguide dimensions for a single-mode operation. The dispersion characteristics of the fundamental TE and TM modes inside the waveguides show that

the nanowires can exhibit zero-dispersion points at the wavelengths of interest. We show that it is possible to minimize the effective mode area and group velocity dispersion by a proper design.

As the next step in this study, the wafer for InGaAsP nanowire have been grown via molecular beam epitaxy (MBE) and the rest of wafers, AlGaAsSb wafers and InGaAsP strip-loaded, have been grown through metalorganic chemical vapour deposition (MOCVD) per our designs. Following the wafer growth, the fabrication of InGaAsP/InP strip-loaded waveguides has been performed. The fabrication technique was based on electron-beam lithography and dry etching.

Finally, the nonlinear optical performance of InGaAsP/InP strip-loaded waveguides has been demonstrated experimentally. We report the first measurement of the nonlinear absorption coefficient of InGaAsP/InP strip-loaded waveguides ($\beta_2 \approx 15$ cm/GW), and the first self-phase modulation (SPM) experiment demonstrating the nonlinear phase shift of up to 2.5π (observed at the coupled-in peak power of 40 W). We have also estimated the nonlinear refractive index of $In_xGa_{1-x}As_yP_{1-y}$/InP with $x = 0.63$ and $y = 0.8$ at the telecom wavelength $\lambda = 1550$ nm to be 10^{-13} cm^2/W. The results of our study suggest that this material might not be the best candidate for all-optical signal processing in the telecom wavelength range, but can be a suitable choice for longer wavelengths where the photon energy lies below the half-bandgap energy of the material. A combination of such waveguides with integrated InGaAsP lasers can potential extend their operation range to beyond 2 μm.

7.1 Future Work

Within this master thesis, we have designed four types of waveguides: strip-loaded waveguides and nanowires based on InGaAsP/InP material platform, and similar waveguide structures based on AlGaAsSb materials. All four wafers for the four waveguide structures have been grown. Due to a limited time frame of the program, we have performed the nonlinear optical characterization of one type of waveguides only, namely: the strip-loaded InGaAsP/InP waveguides. The obvious next step is to perform the waveguide fabrication and nonlinear optical characterization for the remaining three designs: InGaAsP/InP nanowires, and AlGaAsSb strip-loaded waveguides and nanowires. This work is in progress but lies outside the planned work for this thesis. The idea and approaches outlined in this thesis work have paved the way for further assessment of quaternary III-V semiconductor compounds for their nonlinear optical performance.

Semiconductor waveguides are cables routing optical signals on a semiconductor chip. The

waveguides are building blocks of various integrated photonic devices, such as modulators, switches, and converters with suitable applications in telecommunication and other areas. As discussed earlier in the thesis, III-V materials have strong nonlinearity which can make them efficient in nonlinear optical interaction. Additionally, the availability of mature methods for fabrication processes, *e.g.* epitaxial growth and selective etching, offer significant advantages over some rival materials such as, *e.g.*, chalcogenide glass. For these reasons, interest in use of III-V semiconductor waveguides, specifically quaternary compounds for the reasons mentioned earlier, grows continuously. But still, the advantages of these waveguides can become offset by different obstacles, which need to be dealt with. Some of the possible directions of what the continuation of this work can involve are as follow:

- The efficiency of a III-V semiconductor devices for nonlinear optical interactions can be hampered by a high insertion loss. The insertion loss of a device can consequently reduce the transmission length of an optical signal in a communication system, which is highly undesirable. The total end-to-end insertion loss is constituted mostly by coupling loss, propagation loss, and polarization-dependent loss (PDL). Since semiconductor integrated optical devices such as optical waveguides, spot size converters, or multiple quantum well devices are the most generic elements in photonic integrated circuits, it is crucial to have a low insertion loss on the optical path from the laser in free-space or fiber, to the passive waveguides. A study can be conducted to find optimum designs and fabrication approaches for such structures to have low propagation loss and PDL, along with high tolerance to the fiber misalignment with the semiconductor chip.

- The efficiency of III-V semiconductor waveguides rely on other factors beside the insertion loss. One of the greatest obstacles is the large size of semiconductor chips ($\geq$ 1 cm). One of the advantages of III-V integrated devices is the possibility of monolithic integration of them which costs less compared to individual components assembly and hybrid approaches. However, conventional semiconductor devices are usually limited by the bend size [84], and the compromise between the propagation loss and the bend size needs to be found. The trade-off between the propagation loss and bend size of the device can be an important subject to study.

Bibliography

[1] "Cisco Visual Networking Index: Global Mobile Data Traffic Forecast Update, 20162021 White Paper - Cisco - "https://www.cisco.com/c/en/us/solutions/collateral/service-provider/visual-networking-index-vni/mobile-white-paper-c11-520862.html"."

[2] A. E. Willner, S. Khaleghi, M. R. Chitgarha, and O. F. Yilmaz, "All-Optical Signal Processing," *J. Light. Technol.*, vol. 32, pp. 660–680, feb 2014.

[3] M. A. Taubenblatt, "Optical Interconnects for High-Performance Computing," *J. Light. Technol.*, vol. 30, pp. 448–457, feb 2012.

[4] S. Yoo, "Wavelength conversion technologies for WDM network applications," *J. Light. Technol.*, vol. 14, pp. 955–966, jun 1996.

[5] C. Langrock, S. Kumar, J. McGeehan, A. Willner, and M. Fejer, "All-optical signal processing using /spl chi//sup (2)/ nonlinearities in guided-wave devices," *J. Light. Technol.*, vol. 24, pp. 2579–2592, jul 2006.

[6] L. Yan, A. E. Willner, X. Wu, A. Yi, A. Bogoni, Z.-Y. Chen, and H.-Y. Jiang, "All-Optical Signal Processing for UltraHigh Speed Optical Systems and Networks," *J. Light. Technol.*, vol. 30, pp. 3760–3770, dec 2012.

[7] K. Dolgaleva, W. C. Ng, L. Qian, and J. S. Aitchison, "Compact highly-nonlinear AlGaAs waveguides for efficient wavelength conversion," *Opt. Express*, vol. 19, p. 12440, jun 2011.

[8] J. Leuthold, C. Koos, and W. Freude, "Nonlinear silicon photonics," *Nat. Photonics*, vol. 4, pp. 535–544, aug 2010.

[9] A. Liu, L. Liao, D. Rubin, H. Nguyen, B. Ciftcioglu, Y. Chetrit, N. Izhaky, and M. Paniccia, "High-speed optical modulation based on carrier depletion in a silicon waveguide," *Opt. Express*, vol. 15, p. 660, jan 2007.

[10] W. Mathlouthi, H. Rong, and M. Paniccia, "Characterization of efficient wavelength conversion by four-wave mixing in sub-micron silicon waveguides," *Opt. Express*, vol. 16, p. 16735, oct 2008.

[11] S. F. Preble, Q. Xu, B. S. Schmidt, and M. Lipson, "Ultrafast all-optical modulation on a silicon chip," *Opt. Lett.*, vol. 30, p. 2891, nov 2005.

[12] E. Garmire, "Semiconductor Components for Monolithic Applications," pp. 243–304, Springer, Berlin, Heidelberg, 1975.

[13] L. Arizmendi, "Photonic applications of lithium niobate crystals," *Phys. status solidi*, vol. 201, pp. 253–283, jan 2004.

[14] V. G. Ta'eed, M. Shokooh-Saremi, L. Fu, D. J. Moss, M. Rochette, I. C. Littler, B. J. Eggleton, Y. Ruan, and B. Luther-Davies, "Integrated all-optical pulse regenerator in chalcogenide waveguides," *Opt. Lett.*, vol. 30, p. 2900, nov 2005.

[15] V. Ta'eed, M. Shokooh-Saremi, L. Fu, I. Littler, D. Moss, M. Rochette, B. Eggleton, Yinlan Ruan, and B. Luther-Davies, "Self-phase modulation-based integrated optical regeneration in chalcogenide waveguides," *IEEE J. Sel. Top. Quantum Electron.*, vol. 12, pp. 360–370, may 2006.

[16] K. Dolgaleva, P. Sarrafi, P. Kultavewuti, K. M. Awan, N. Feher, J. S. Aitchison, L. Qian, M. Volatier, R. Arès, and V. Aimez, "Tuneable four-wave mixing in AlGaAs nanowires," *Opt. Express*, vol. 23, p. 22477, aug 2015.

[17] P. Kultavewuti, V. Pusino, M. Sorel, and J. Stewart Aitchison, "Low-power continuous-wave four-wave mixing wavelength conversion in AlGaAs-nanowaveguide microresonators," *Opt. Lett.*, vol. 40, p. 3029, jul 2015.

[18] P. Apiratikul, J. J. Wathen, G. A. Porkolab, B. Wang, L. He, T. E. Murphy, and C. J. K. Richardson, "Enhanced continuous-wave four-wave mixing efficiency in nonlinear AlGaAs waveguides.," *Opt. Express*, vol. 22, pp. 26814–24, nov 2014.

[19] J. Aitchison, D. Hutchings, J. Kang, G. Stegeman, and A. Villeneuve, "The nonlinear optical properties of AlGaAs at the half band gap," *IEEE J. Quantum Electron.*, vol. 33, pp. 341–348, mar 1997.

[20] "The Nobel Prize in Physics 2000 - "https://www.nobelprize.org/nobel_prizes/physics/laureates/2000/"."

[21] "The Nobel Prize in Physics 2014 - "https://www.nobelprize.org/nobel_prizes/physics/laureates/2014/"."

[22] "Industrial Semiconductor Market Tracker - Q3 2016 - IHS Technology - "https://technology.ihs.com/580001/industrial-semiconductor-market-tracker-q3-2016"."

[23] "Industrial chip market on a roll - "https://www.electronicsweekly.com/market-sectors/industrial-electronics/industrial-chip-market-roll-2015-03/"."

[24] J. Donnelly, H. Le, E. Swanson, S. Groves, A. Darwish, and E. Ippen, "Nondegenerate four-wave mixing wavelength conversion in low-loss passive InGaAsP-InP quantum-well waveguides," *IEEE Photonics Technol. Lett.*, vol. 8, pp. 623–625, may 1996.

[25] M. Dinu, F. Quochi, and H. Garcia, "Third-order nonlinearities in silicon at telecom wavelengths," *Appl. Phys. Lett.*, vol. 82, pp. 2954–2956, may 2003.

[26] R. W. Boyd, *Nonlinear optics*. Academic Press, 3 ed., apr 2008.

[27] J. Bardeen and W. H. Brattain, "The Transistor, A Semi-Conductor Triode," *Phys. Rev.*, vol. 74, pp. 230–231, jul 1948.

[28] N. Holonyak, "From transistors to light emitters," *IEEE J. Sel. Top. Quantum Electron.*, vol. 6, pp. 1190–1200, nov 2000.

[29] F. A. Kish, D. Welch, R. Nagarajan, J. L. Pleumeekers, V. Lal, M. Ziari, A. Nilsson, M. Kato, S. Murthy, P. Evans, S. W. Corzine, M. Mitchell, P. Samra, M. Missey, S. DeMars, R. P. Schneider, M. S. Reffle, T. Butrie, J. T. Rahn, M. Van Leeuwen, J. W. Stewart, D. J. Lambert, R. C. Muthiah, H. Tsai, J. S. Bostak, A. Dentai, K. Wu, H. Sun, D. J. Pavinski, J. Zhang, J. Tang, J. McNicol, M. Kuntz, V. Dominic, B. D. Taylor, R. A. Salvatore, M. Fisher, A. Spannagel, E. Strzelecka, P. Studenkov, M. Raburn, W. Williams, D. Christini, K. K. Thomson, S. S. Agashe, R. Malendevich, G. Goldfarb, S. Melle, C. Joyner, M. Kaufman, and S. G. Grubb, "Current Status of Large-Scale InP Photonic Integrated Circuits," *IEEE J. Sel. Top. Quantum Electron.*, vol. 17, pp. 1470–1489, nov 2011.

[30] K. Tsuzuki, T. Ishibashi, T. Ito, S. Oku, Y. Shibata, T. Ito, R. Iga, Y. Kondo, and Y. Tohmori, "A 40-gb/s InGaAlAs-InAlAs MQW n-i-n Mach-Zehnder Modulator with a drive Voltage of 2.3 V," *IEEE Photonics Technol. Lett.*, vol. 17, pp. 46–48, jan 2005.

[31] F. Kish, R. Nagarajan, D. Welch, P. Evans, J. Rossi, J. Pleumeekers, A. Dentai, M. Kato, S. Corzine, R. Muthiah, M. Ziari, R. Schneider, M. Reffle, T. Butrie, D. Lambert, M. Missey, V. Lal, M. Fisher, S. Murthy, R. Salvatore, S. Demars, A. James, and C. Joyner, "From Visible

Light-Emitting Diodes to Large-Scale IIIV Photonic Integrated Circuits," *Proc. IEEE*, vol. 101, pp. 2255–2270, oct 2013.

[32] S. Strite, "GaN, AlN, and InN: A review," *J. Vac. Sci. Technol. B Microelectron. Nanom. Struct.*, vol. 10, p. 1237, jul 1992.

[33] S. Mohammad, A. Salvador, and H. Morkoc, "Emerging gallium nitride based devices," *Proc. IEEE*, vol. 83, no. 10, pp. 1306–1355, 1995.

[34] S. G. Stan, *The CD-ROM drive : a brief system description.* Kluwer Academic Publishers, 1998.

[35] Y. J. Tsao, *The World of Compound Semiconductors.*

[36] S. Adachi, *Properties of semiconductor alloys : group-IV, III-V and II-VI semiconductors.* Wiley, 2009.

[37] S. Adachi, "Band gaps and refractive indices of AlGaAsSb, GaInAsSb, and InPAsSb: Key properties for a variety of the 24μm optoelectronic device applications," *J. Appl. Phys.*, vol. 61, pp. 4869–4876, may 1987.

[38] J. Piprek, T. Peng, G. Qui, and J. Olowolafe, "Energy gap bowing and refractive index spectrum of AlInN and AlGaInN," in *Compd. Semicond. 1997. Proc. IEEE Twenty-Fourth Int. Symp. Compd. Semicond.*, pp. 227–230, IEEE.

[39] B. E. Saleh, M. C. Teich, and B. Saleh, *Fundamentals of photonics.* New York: Wiley, 1991.

[40] A. R. Denton and N. W. Ashcroft, "Vegard's law," *Phys. Rev. A*, vol. 43, pp. 3161–3164, mar 1991.

[41] P. Werle, F. Slemr, K. Maurer, R. Kormann, R. Mücke, and B. Jänker, "Near- and mid-infrared laser-optical sensors for gas analysis," *Opt. Lasers Eng.*, vol. 37, pp. 101–114, feb 2002.

[42] M. Lončar, A. Scherer, and Y. Qiu, "Photonic crystal laser sources for chemical detection," *Appl. Phys. Lett.*, vol. 82, pp. 4648–4650, jun 2003.

[43] S. D. Gunapala, B. F. Levine, D. Ritter, R. A. Hamm, and M. B. Panish, "Latticematched InGaAsP/InP longwavelength quantum well infrared photodetectors," *Appl. Phys. Lett.*, vol. 60, pp. 636–638, feb 1992.

[44] A. Zussman, B. F. Levine, J. M. Kuo, and J. de Jong, "Extended longwavelength λ=1115μm GaAs/Al x Ga 1 x As quantumwell infrared photodetectors," *J. Appl. Phys.*, vol. 70, pp. 5101–5107, nov 1991.

[45] B. F. Levine, S. D. Gunapala, and R. F. Kopf, "Photovoltaic GaAs quantum well infrared detectors at 4.2 μm using indirect Al x Ga 1 x barriers," *Appl. Phys. Lett.*, vol. 58, pp. 1551–1553, apr 1991.

[46] E. Innerhofer, F. Brunner, S. V. Marchese, R. Paschotta, G. Arisholm, S. Kurimura, K. Kitamura, T. Usami, H. Ito, and U. Keller, "Analysis of nonlinear wavelength conversion system for a redgreenblue laser-projection source,"

[47] J. Meier, W. S. Mohammed, A. Jugessur, L. Qian, M. Mojahedi, and J. S. Aitchison, "Group velocity inversion in AlGaAs nanowires," *Opt. Express*, vol. 15, p. 12755, oct 2007.

[48] G. P. Agrawal, "Nonlinear Fiber Optics," in *Nonlinear Sci. Daw. 21st Century*, pp. 195–211, Berlin, Heidelberg: Springer Berlin Heidelberg.

[49] W. D. Callister and D. G. Rethwisch, *Materials science and engineering : an introduction*. Wiley, 9th ed.

[50] E. Kuphal and E., "Phase diagrams of InGaAsP, InGaAs and InP lattice-matched to (100)InP," *J. Cryst. Growth*, vol. 67, pp. 441–457, aug 1984.

[51] M. Feng, L. W. Cook, M. M. Tashima, and G. E. Stillman, "Lattice constant, bandgap, thickness, and surface morphology of InGaAsP-InP layers grown by step-cooling, equilibrium-cooling, supercooling and two-phase-solution growth techniques," *J. Electron. Mater.*, vol. 9, pp. 241–280, mar 1980.

[52] A. Sasaki, M. Nishiuma, and Y. Takeda, "Energy Band Structure and Lattice Constant Chart of III-V Mixed Semiconductors, and AlGaSb/AlGaAsSb Semiconductor Lasers on GaSb Substrates," *Jpn. J. Appl. Phys.*, vol. 19, pp. 1695–1702, sep 1980.

[53] J. Limpert, T. Schreiber, S. Nolte, H. Zellmer, T. Tunnermann, R. Iliew, F. Lederer, J. Broeng, G. Vienne, A. Petersson, and C. Jakobsen, "High-power air-clad large-mode-area photonic crystal fiber laser," *Opt. Express*, vol. 11, p. 818, apr 2003.

[54] N. Broderick, H. Offerhaus, D. Richardson, R. Sammut, J. Caplen, and L. Dong, "Large Mode Area Fibers for High Power Applications," *Opt. Fiber Technol.*, vol. 5, pp. 185–196, apr 1999.

[55] B. Eggleton, T. Vo, R. Pant, J. Schr, M. Pelusi, D. Yong Choi, S. Madden, and B. Luther-Davies, "Photonic chip based ultrafast optical processing based on high nonlinearity dispersion engineered chalcogenide waveguides," *Laser Photon. Rev.*, vol. 6, pp. 97–114, jan 2012.

[56] D. Duchesne, R. Morandotti, G. A. Siviloglou, R. El-Ganainy, G. I. Stegeman, D. N. Christodoulides, D. Modotto, A. Locatelli, C. De Angelis, F. Pozzi, and M. Sorel, "Nonlinear Photonics in AlGaAs Photonics Nanowires: Self Phase and Cross Phase Modulation," in *2007 Int. Symp. Signals, Syst. Electron.*, pp. 475–478, IEEE, jul 2007.

[57] Z. Zang and Y. Zhang, "Analysis of optical switching in a Yb^3+-doped fiber Bragg grating by using self-phase modulation and cross-phase modulation," *Appl. Opt.*, vol. 51, p. 3424, jun 2012.

[58] F. Parmigiani, C. Finot, K. Mukasa, M. Ibsen, M. A. Roelens, P. Petropoulos, and D. J. Richardson, "Ultra-flat SPM-broadened spectra in a highly nonlinear fiber using parabolic pulses formed in a fiber Bragg grating," *Opt. Express*, vol. 14, p. 7617, aug 2006.

[59] R. Stolen and J. Bjorkholm, "Parametric amplification and frequency conversion in optical fibers," *IEEE J. Quantum Electron.*, vol. 18, pp. 1062–1072, jul 1982.

[60] A. Yariv and D. M. Pepper, "Amplified reflection, phase conjugation, and oscillation in degenerate four-wave mixing," *Opt. Lett.*, vol. 1, p. 16, jul 1977.

[61] S. Coen, A. H. L. Chau, R. Leonhardt, J. D. Harvey, J. C. Knight, W. J. Wadsworth, and P. S. J. Russell, "Supercontinuum generation by stimulated Raman scattering and parametric four-wave mixing in photonic crystal fibers," *J. Opt. Soc. Am. B*, vol. 19, p. 753, apr 2002.

[62] J. O. White and A. Yariv, "Realtime image processing via fourwave mixing in a photorefractive medium," *Appl. Phys. Lett.*, vol. 37, pp. 5–7, jul 1980.

[63] N. J. D. NAGELKERKE, "A note on a general definition of the coefficient of determination," *Biometrika*, vol. 78, pp. 691–692, sep 1991.

[64] J. L. Zilko, *"Metal organic chemical vapor deposition: technology and equipment." Handbook of thin-film deposition processes and techniques : principles, methods, equipment and applications.* Noyes Publications/William Andrew Pub, 2002.

[65] R. Pelzel, "A Comparison of MOVPE and MBE Growth Technologies for III-V Epitaxial Structures," (New Orleans, Louisiana, USA), CS MANTECH Conference, 2013.

[66] W. S. Kondle and R. Chow, *Molecular beam epitaxy: Equipment and practice. HANDBOOK OF THIN-FILM DEPOSITION PROCESSES AND TECHNIQUES.* Noyes Publications/William Andrew Pub, 2002.

[67] G. Tittelbach, B. Richter, and W. Karthe, "Comparison of three transmission methods for integrated optical waveguide propagation loss measurement," *Pure Appl. Opt. J. Eur. Opt. Soc. Part A*, vol. 2, pp. 683–700, nov 1993.

[68] H. K. Tsang, C. S. Wong, T. K. Liang, I. E. Day, S. W. Roberts, A. Harpin, J. Drake, and M. Asghari, "Optical dispersion, two-photon absorption and self-phase modulation in silicon waveguides at 1.5 μm wavelength," *Appl. Phys. Lett.*, vol. 80, pp. 416–418, jan 2002.

[69] H. K. Tsang, R. V. Penty, I. H. White, R. S. Grant, W. Sibbett, J. B. D. Soole, H. P. LeBlanc, N. C. Andreadakis, R. Bhat, and M. A. Koza, "Twophoton absorption and selfphase modulation in InGaAsP/InP multiquantumwell waveguides," *J. Appl. Phys.*, vol. 70, pp. 3992–3994, oct 1991.

[70] B. Jensen and A. Torabi, "Refractive index of quaternary In 1 x Ga x As y P 1 y lattice matched to InP," *J. Appl. Phys.*, vol. 54, pp. 3623–3625, jun 1983.

[71] E. D. Palik, *Handbook of optical constants of solids.* Academic Press, 1985.

[72] S. Saeidi, K. M. Awan, L. Sirbu, and K. Dolgaleva, "Nonlinear photonics on-a-chip in III-V semiconductors: quest for promising material candidates," *Appl. Opt.*, vol. 56, p. 5532, jul 2017.

[73] R. L. Sutherland, "Handbook of nonlinear optics," 2003.

[74] M. Bass, E. W. Van Stryland, D. R. Williams, and W. L. Wolfe, *Handbook of optics.* McGraw-Hill, 1995.

[75] G. Stegeman, A. Villeneuve, J. Kang, J. Aitchison, C. Ironside, K. Al-Heymari, C. Yang, C.-H. Lin, H.-H. Lin, G. Kennedy, R. Grant, and W. Sibbett, "AlGaAs BELOW HALF BANDGAP: THE SILICON OF NONLINEAR OPTICAL MATERIALS," *J. Nonlinear Optic. Phys. Mat.*, vol. 3, p. 347, july 1994.

[76] P. A. Andrekson, N. A. Olsson, J. R. Simpson, T. Tanbun-Ek, R. A. Logan, and M. Haner, "All-Optical Demultiplexing at 16 Gbit/s using Four-Wave Mixing," in *Opt. Fiber Commun.*, (Washington, D.C.), p. PD5, OSA, feb 1991.

[77] S. Kawanishi and O. Kamatani, "All-optical time division multiplexing using four-wave mixing," *Electron. Lett.*, vol. 30, pp. 1697–1698, sep 1994.

[78] V. Vusirikala, S. Saini, R. Bartolo, R. Whaley, S. Agarwala, M. Dagenais, F. Johnson, and D. Stone, "High butt-coupling efficiency to single-mode fibers using a 1.55-μm InGaAsP laser integrated with a tapered ridge mode transformer," *IEEE Photonics Technol. Lett.*, vol. 9, pp. 1472–1474, nov 1997.

[79] I. Moerman, P. Van Daele, and P. Demeester, "A review on fabrication technologies for the monolithic integration of tapers with III-V semiconductor devices," *IEEE J. Sel. Top. Quantum Electron.*, vol. 3, no. 6, pp. 1308–1320, 1997.

[80] V. I. Tolstikhin, F. Wu, Y. Logvin, A. Densmore, K. Pimenov, and S. Grabtchak, "InP-based photonic integrated circuits for optical performance surveillance, signal conditioning, and bandwidth management in DWDM transmission systems," vol. 5579, p. 522, International Society for Optics and Photonics, nov 2004.

[81] F. Wu, V. I. Tolstikhin, A. Densmore, and S. Grabtchak, "On-chip spot-size converter using a two-step lateral taper for efficient coupling to {InP}-based photonic integrated circuits," in *Tech. Dig. Integr.\ Photon.\ Res.*, p. JWB23, 2004.

[82] S. Preble, M. Lipson, and H. Lipson, "Two-dimensional photonic crystals designed by evolutionary algorithms," *Appl. Phys. Lett.*, vol. 86, p. 061111, feb 2005.

[83] B. J. Offrein, D. Erni, G.-L. Bona, I. Massarek, M. M. Hler, and R. Germann, "A Very Short Planar Silica Spot-Size Converter Using a Nonperiodic Segmented Waveguide," *J. Light. Technol. Vol. 16, Issue 9, pp. 1680-*, vol. 16, p. 1680, sep 1998.

[84] R. Deri and E. Kapon, "Low-loss III-V semiconductor optical waveguides," *IEEE J. Quantum Electron.*, vol. 27, pp. 626–640, mar 1991.